



HHS Public Access

Author manuscript

Mol Cell. Author manuscript; available in PMC 2021 September 27.

Published in final edited form as:

Mol Cell. 2021 September 02; 81(17): 3468–3480.e7. doi:10.1016/j.molcel.2021.06.032.

Solenoid architecture of HUWE1 contributes to ligase activity and substrate recognition

Moritz Hunkeler^{1,2}, Cyrus Y. Jin^{1,2}, Michelle W. Ma^{1,2}, Julie K. Monda³, Daan Overwijn¹, Eric J. Bennett³, Eric S. Fischer^{1,2,4,*}

¹Department of Cancer Biology, Dana-Farber Cancer Institute, Boston, MA 02215, USA

²Department of Biological Chemistry and Molecular Pharmacology, Harvard Medical School, Boston, MA 02115, USA

³Division of Biological Sciences, Section of Cell and Developmental Biology, University of California, San Diego, La Jolla, CA 92093, USA

⁴Lead contact

SUMMARY

HECT ubiquitin ligases play essential roles in metazoan development and physiology. The HECT ligase HUWE1 is central to the cellular stress response by mediating degradation of key death or survival factors, including Mc11, p53, DDIT4, and Myc. Although mutations in HUWE1 and related HECT ligases are widely implicated in human disease, our molecular understanding remains limited. Here we present a comprehensive investigation of full-length HUWE1, deepening our understanding of this class of enzymes. The N-terminal ~3,900 amino acids of HUWE1 are indispensable for proper ligase function, and our cryo-EM structures of HUWE1 offer a complete molecular picture of this large HECT ubiquitin ligase. HUWE1 forms an alpha solenoid-shaped assembly with a central pore decorated with protein interaction modules. Structures of HUWE1 variants linked to neurodevelopmental disorders as well as of HUWE1 bound to a model substrate link the functions of this essential enzyme to its three-dimensional organization.

Graphical Abstract

This is an open access article under the CC BY-NC-ND license (<http://creativecommons.org/licenses/by-nc-nd/4.0/>).

*Correspondence: eric_fischer@dfci.harvard.edu.

AUTHOR CONTRIBUTIONS

M.H. and E.S.F. designed the research plan. M.H. cloned and purified proteins, prepared EM grids, collected data, and determined structures. C.Y.J. purified proteins and established, conducted, and analyzed E3 activity assays. M.W.M. established, conducted, and analyzed E2 discharge assays. M.W.M. and D.O. purified HUWE1^{HECT}. D.O. assisted with cloning. J.K.M. established, conducted, and analyzed all cellular assays. All authors contributed to experimental design and analyzed and interpreted data. M.H. prepared figures. E.J.B. and E.S.F. conceived and supervised the study and acquired funding. M.H. and E.S.F. wrote the manuscript with input from all authors. All authors approved the final version of the manuscript.

SUPPLEMENTAL INFORMATION

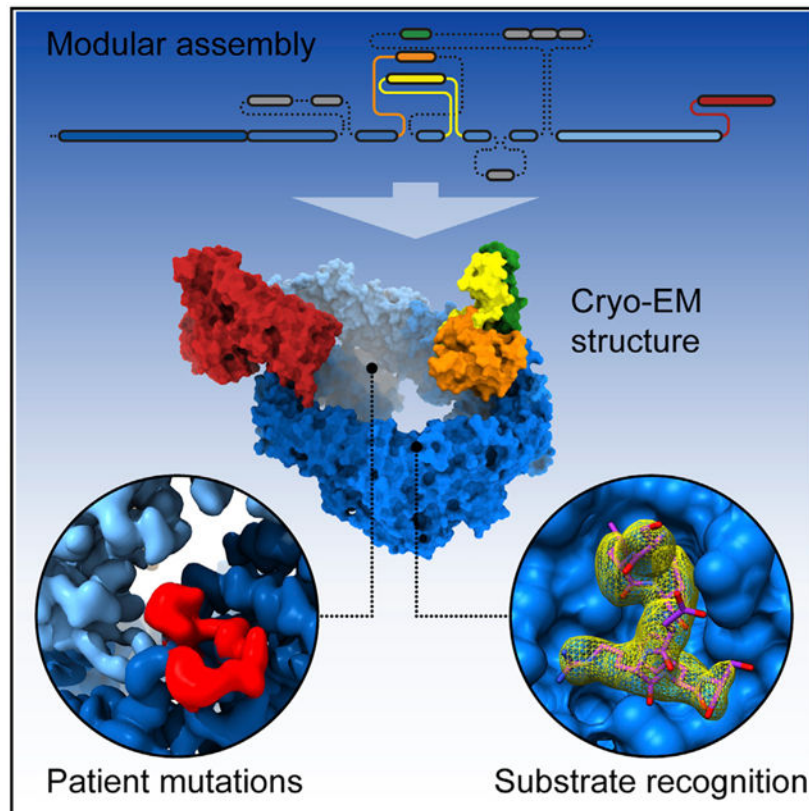
Supplemental information can be found online at <https://doi.org/10.1016/j.molcel.2021.06.032>.

DECLARATION OF INTERESTS

E.S.F. is a founder, scientific advisory board (SAB) member, and equity holder of Civetta Therapeutics, Jengu Therapeutics (board member), and Neomorph, Inc. E.S.F. is an equity holder in C4 Therapeutics and a consultant to Novartis, Sanofi, EcoR1 Capital, Deerfield, and Astellas. The Fischer lab receives or has received research funding from Novartis, Ajax, and Astellas.

SUPPORTING CITATIONS

The following references appear in the Supplemental information: Tan et al. (2017).



In brief

Hunkeler et al. present the cryo-EM structure of HUWE1, a large HECT E3 ligase that forms a modular ring-shaped assembly with flexibly attached accessory domains. The influence of mutations associated with intellectual disabilities on HUWE1 activity and substrate recognition by HUWE1 is dissected biochemically and structurally.

INTRODUCTION

The covalent modification of proteins with ubiquitin (ubiquitylation) is an essential process carried out by a three-enzyme cascade consisting of E1 (ubiquitin activating), E2 (ubiquitin conjugating), and E3 (ubiquitin ligase) enzymes (Hershko and Ciechanover, 1998; Komander and Rape, 2012; O’Connell and Harper, 2007). E3 ubiquitin ligases confer specificity to the process of ubiquitylation and fall into three major classes: RING (really interesting new gene), RBR (ring-between-ring), and HECT ligases (Zheng et al., 2017). HECT (homologous to the E6-AP carboxyl terminus) ligases, which can have large and complex architectures, are unique in their catalytic mechanism (Lorenz, 2018), frequently mutated in developmental disorders, and widely implicated in carcinogenesis (Bernassola et al., 2019; Moortgat et al., 2018; Wang et al., 2020). The human genome encodes for 28 HECT ligases, all containing the name giving conserved C-terminal HECT domain. The HECT domain consists of an N-lobe, which is responsible for E2 binding, and a smaller, flexible C-lobe, which contains a catalytic cysteine residue. During ubiquitylation, ubiquitin

is transferred from an E2 to the active site cysteine prior to transfer to a substrate lysine. The regions N-terminal to the HECT domain are diverse among family members, ranging in molecular weights from ~40 to ~490 kDa, and harbor a multitude of additional accessory domains (Lorenz, 2018). Although these N-terminal regions are believed to be responsible for regulation, substrate recognition, and linkage specificity, the lack of structural data on full-length HECT ligases limits our mechanistic understanding (Lorenz, 2018). Structural studies of isolated HECT domains, in particular studies on the NEDD4-type subfamily HECT domain with up to ~100 preceding regulatory amino acids (Kamadurai et al., 2009, 2013; Zhu et al., 2017), have shed light on the catalytic mechanism of HECT ligases, but it remains largely elusive how the extended N-terminal regions contribute to activity and regulation.

The large (~480 kDa) HECT family member HUWE1 (HECT, UBA, and WWE domain containing protein 1), which is also known in the literature as Mule/ARF-BP1/LASU1/HECTH9/URE-B1/E3Histone, was initially shown to degrade three key regulators of stress response and survival pathways: Mcl1, p53, and c-Myc (Adhikary et al., 2005; Chen et al., 2005; Zhong et al., 2005). A growing list of HUWE1 substrates has since been reported (Kao et al., 2018), including the stress-responsive regulator of mTORC1 signaling, DDIT4 (Brugarolas et al., 2004; Thompson et al., 2014), and many DNA damage response factors, such as the BRCA1 tumor suppressor, TopBP1, Cdc6, and CHEK1 (Cassidy et al., 2020; Hall et al., 2007; Herold et al., 2008; Wang et al., 2014). Loss of HUWE1 sensitizes cells not only to DNA damage but also to a variety of other stressors, including both oxidative and hypoxic stress (Amici et al., 2019; Bosshard et al., 2017; Clements et al., 2019; Kao et al., 2018; Olivieri et al., 2020). In addition, HUWE1 has been shown to mediate the destruction of unassembled constituents of multi-protein complexes and free histones (Liu et al., 2005; Singh et al., 2009a, 2009b; Xu et al., 2016), contributing to protein quality control (Sung et al., 2016; Xu et al., 2016) and cell cycle checkpoint decisions.

Micro-duplications and splice-site or missense mutations of the HUWE1 gene are associated with X-linked intellectual disability (ID) and developmental disorders (Giles and Grill, 2020; Moortgat et al., 2018). Although increased gene dosage has been linked with mild to moderate ID with speech delay, missense variants are linked with severe ID in males and also females, despite preferential inactivation of the affected X chromosome (Moortgat et al., 2018). Common symptoms in affected patients include global developmental delay, post-natal short stature, and dysmorphic facial features. Whole HUWE1 deletions have not been reported so far, and truncated variants are very rare, in line with the HUWE1 gene's being classified as highly essential with a loss-of-function intolerance of 1.0 (Moortgat et al., 2018). The functional impact of reported patient mutations on HUWE1 activity is not well understood.

All these findings suggest that HUWE1 is a ubiquitin ligase critically involved in a multitude of essential cellular pathways and raise the question of how HUWE1 engages with such a large number of substrates in a regulated manner. Atomic structures of the catalytic HECT domain of HUWE1 have provided insights into its mechanism, but these structures lack the ~3,900 N-terminal amino acids of HUWE1 believed to be critical for substrate recruitment and regulation (Pandya et al., 2010). The structure of a HUWE1 construct that spans the

HECT domain and about ~50 amino acids N-terminal to the HECT domain has revealed an asymmetric dimer configuration involving two helices N-terminal to the HECT domain. These two helices, termed the “dimerization region” (DR) (Sander et al., 2017), were proposed to be involved in HUWE1 regulation through an unprecedented mechanism of autoinhibitory dimerization. It was further shown that this autoinhibitory interaction can be alleviated by intramolecular interactions with the so-called activation segment (AS) (Sander et al., 2017), together suggesting a model for HUWE1 regulation. Most biochemical studies of HUWE1, including work testing the autoinhibition model, have only been performed with truncated HUWE1 proteins lacking the entire N-terminal region (Lee et al., 2019; Pandya et al., 2010; Sander et al., 2017), and further understanding of this important ligase necessitates a molecular understanding of HUWE1 activity in the context of the full-length protein.

To assess how the large N-terminal region of HUWE1 contributes to activity and regulation of HUWE1 and how HUWE1 can engage with such a diverse set of substrates, we purified and determined the structure of full-length HUWE1. We demonstrate that the N-terminal region is critical for ligase activity and substrate recruitment, and the first atomic model of a full-length HECT E3 ligase reveals a unique modular ring-shaped E3 ligase architecture. We show how a combination of distinct binding domains and peptide interactions with the scaffolding armadillo repeats contribute to substrate recruitment and reconcile previous observations in the context of the fully assembled enzyme.

RESULTS

N-terminal region of HUWE1 is critical for ligase loading and E3 activity

The N-terminal region of HUWE1 consists of expanded sets of helical armadillo repeats, several ubiquitin binding domains, a poly-ADP ribose (PAR) binding WWE domain, an Mcl1-binding BH3 domain and a large (~900 amino acids [aa]) disordered region (Figure 1A). We cloned full-length HUWE1 and overexpressed and purified it from Expi293 mammalian cells to high purity (Figure S1). To functionally dissect HUWE1 activity, we established assays to monitor both the loading of HUWE1 with ubiquitin as well as the overall E3 ligase activity. A single-turnover E2 discharge assay was established on the basis of previously published methods (Kamadurai et al., 2013), and we used two well-established HUWE1 substrates, Mcl1 (Zhong et al., 2005) and DDIT4 (Thompson et al., 2014), for ubiquitylation assays and as proxies for readout of general HUWE1 activity (Figures S1B and S1C). We first compared overall activity of full-length HUWE1 with an isolated HECT domain construct (HUWE1_{HECT}, aa 3993–4374). Full-length HUWE1 shows significantly higher activity than HUWE1_{HECT} with respect to Mcl1 and DDIT4 ubiquitination (Figures 1B and 1C), suggesting that the activity observed with the isolated HECT domain likely represents unspecific background activity. We next asked whether the presence of the N-terminal region is also important for ligase loading by following the kinetics of ubiquitin transfer from a ubiquitin-charged E2 (E2-Ub) to HUWE1. We show that HUWE1_{HECT} is, in our experimental settings, inefficiently loaded by E2-Ub compared with full-length HUWE1 (Figures 1D and 1E). In fact, the level of E2 discharge is indistinguishable from assays with a catalytically dead Cys4341-to-Ser mutant (C4341S). These results illustrate the importance

of the N-terminal region for both ligase loading as well as ubiquitin conjugation activity and raise the question of how the N-terminal domains contribute functionally.

HUWE1 adopts a ring-shaped architecture

To structurally understand how the N-terminal domains of HUWE1 cooperate with the HECT domain, we pursued cryoelectron microscopy (cryo-EM) using the full-length HUWE1 protein. Initial high-quality two-dimensional (2D) class averages from a dataset collected on a Talos Arctica (Thermo Fisher Scientific) revealed substantial conformational heterogeneity, displaying two distinct states that appear as a “closed” ring-like architecture as well as an apparently continuous “open” conformation (Figure 1F). Since continuous flexibility can prohibit high-resolution structure determination, we used chemical crosslinking (BS3 crosslinker) to stabilize HUWE1 (Figures S1D and S1E) and collected datasets on a Titan Krios (Thermo Fisher Scientific) for both BS3-crosslinked and non-crosslinked HUWE1. BS3 crosslinking enriched for the closed ring conformation, and a consensus reconstruction was refined to an overall resolution of ~ 3.1 Å (ranging from 3 to 6 Å), judged using the Fourier shell correlation (FSC) = 0.143 threshold criterion (Figures 2 and S2-S4). A reconstruction of “closed” particles from the non-crosslinked dataset was refined to an overall resolution of ~ 3.4 Å (ranging from 3 to 9 Å) (Figure S5). The resulting maps showed nearly indistinguishable structures for the closed conformation (Figures 2 and S2-S5), and we therefore focus here on the better defined map from the BS3-crosslinked sample. The cryo-EM density in the helical repeat region allowed manual building of an atomic model, while crystal structures of the HECT and the WWE domains were available for the less well defined regions (Figures 2B-2D and S4; Table S1).

The central feature of HUWE1 is a large alpha solenoid structure with dimensions of $\sim 140 \times \sim 100 \times 100$ Å. It is built from four helical armadillo repeat-like domains (ARLD1–4), of which two, ARLD1 (aa 1–840) and ARLD2 (aa 841–1610), were previously identified on the basis of sequence analysis (Zhong et al., 2005). Together with ARLD3 (aa 1750–2259) and ARLD4 (aa 3179–3989), these form a ring-shaped solenoid with an inner circumference of ~ 250 Å (Figure 2). This ring is decorated with accessory modules that are inserted in or between the helical repeat domains (Figures 1A and 2B-2D). Specifically, the ubiquitin binding UBA and UIM domains (“UB module 1,” aa 1317–1390) are inserts into ARLD2; they are flexibly tethered to the ring by linkers of 27 and 42 residues. Although not visible in our cryo-EM maps, the UB module 1 is constrained topologically to lie above the plane of the ring (Figures 2B and 2C). The WWE domain (aa 1611–1683), which also lies above the plane of the ring, follows ARLD2 (Figures 2B-2D, S4I, and S4J). It interacts with a previously uncharacterized domain (aa 1831–1938; Figures 2B-2D, 3A, and S4I), inserted into ARLD3, which we termed the “HWA” domain (HUWE1 WWE module associated). The Mcl1-binding BH3 domain (aa 1976–1991), which lies below the ring, is also an insert into the ARLD3. Like the UB modules, the BH3 domain is not visible in our cryo-EM reconstructions (Figures 2D and 3A). A largely disordered region spans residues 2259–3179 between ARLD3 and ARLD4, only featuring one folded helix-turn-helix motif (“Tower,” aa 2641–2696; Figures 1A, 3A, S4H, and S4I) and a UBM domain consisting of three repetitive elements (“UB module 2,” aa 2951–3100; Figures 1A, 2C, 2D, 3A, and 3B). The

Tower motif is found tightly sandwiched between the WWE and HWA domains (“WWE module”; Figures 1A, 2B-2D, 3A, and S4I).

HUWE1 architecture is important for activity

The alpha solenoid architecture is established by a ring-closure interface that comprises residues of the ARLD1 and the ARLD4 domains (Figures 3B-3D), with a total interface area of $\sim 860 \text{ \AA}^2$. Two structural motifs are the principal features of the contact. In one, Tyr355 and His356, in a helix-loop-helix motif in ARLD1, are buried in a largely hydrophobic groove in the ARLD4 domain (Figure 3C). In the other, an extended loop (aa 3288–3299) with Leu3294 at its tip protrudes from the ARLD4 domain into a hydrophobic pocket in the ARLD1 domain (Figure 3D). Although we cannot exclude the possibility that the open state is an artifact of the cryo-grid preparation known to frequently lead to “broken” particles, the presence of the open conformation in the non-crosslinked dataset (Figure S3; Video S1) prompted us to investigate whether perturbations to the ring-closure interface would affect activity. Consistent with the functional importance of the closed architecture, mutations in the helix-loop-helix motif (Y355G/H356G, “YH/GG”) as well as deletion of the hydrophobic loop (3291–3298) decreased E3 activity of HUWE1 (Figure S6A). A combination of the two mutations leads to an additive decrease in activity and decreases the apparent E2 discharge (Figures 4A and 4B). These results suggest that the closed conformation of HUWE1 is necessary for full activity of HUWE1.

The HECT domain is flexibly tethered to the ring

The HECT domain displays a high degree of flexibility, leading to blurred density in the consensus refinement (Figure S2) that can also be visualized by structural variance analysis (Video S2). Masked classification reveals an enriched subpopulation in the data where the HECT domain sits right above the plane of the ring nestled on top of ARLD1 but without extensive direct contacts to the repeat domains of the ring (total interface area $\sim 400 \text{ \AA}^2$). The crystal structure of the HECT domain was readily docked into the density (Figure S4G), and although it represents only a subset of the particles, we use this conformation for illustration and further discussion. Structures of isolated HECT domains in complex with E2 (Kamadurai et al., 2009) and substrate peptides (Kamadurai et al., 2013) have established a catalytic mechanism of HECT ubiquitin ligases that requires the HECT domain to run through distinct states of a catalytic cycle (Lorenz, 2018). These states are defined by the relative orientation of the C-lobe with respect to the N-lobe (Figure S7). In our structure, the HECT domain is found in a resting or inactive conformation, which is compatible with transition into the T-state/E2-binding state (Figures S7A and S7B). However, the observed enriched subpopulation would not allow transition to the C-lobe into the ubiquitin transfer-competent L-state without major clashes with the ARLD1 (Figure S7C), which implies that the HECT domain must undergo conformational rearrangements consistent with the flexibility observed in our reconstructions. The basis for this flexibility appears rooted in the connection between the HECT domain and the ARLD4. The two domains are linked by a hinge-like interface made up of a 3-3 helix-bundle (Figure 4C). The two sets of three helices (aa 3851–3893 and 3953–3986, respectively) are connected by a disordered linker (aa 3894–3952). Strikingly, the constituents of the helical bundle are the previously identified DR on the HECT side and the AS on the ARLD4 side (Sander et al., 2017). In the context of

an N-terminally truncated HUWE1, previous studies had shown that the DR facilitates an auto-inhibited state of HUWE1, and increased activity was observed upon introduction of mutations in the DR that disrupt the auto-inhibited dimer (Sander et al., 2017). It was further shown that the AS forms a transient intramolecular interaction with the DR that antagonizes dimerization, and thereby the presence of the AS leads to increased activity. Although we do not observe dimerization of full-length HUWE1, our observations are consistent with the importance of the transient interface formed by the 3-3 helix-bundle consisting of DR and AS. The flexible linker between DR and AS allows the HECT to access a large area upon release of the 3-3 helix bundle. To reconcile the role of this transient interface and the linker in the context of the full-length HUWE1 protein, we took advantage of the mutations in the DR that have been shown to disrupt this interface (Sander et al., 2017) (I3969A/F3982A and H3962D). In contrast to what has been observed for the truncated construct (Sander et al., 2017), we observe that both mutations show lower activity in ligase loading as assessed by the E2 discharge assay (Figure 4D) and are also impaired in the E3 ligase assay (Figure 4A). In addition, deletion of the linker (3896–3951) also leads to impairment of ligase activity and loading (Figures 4A and 4D). These findings combined suggest that both the observed conformation of the 3-3 helix bundle and the apparent mobility of the HECT domain, governed by the transient nature of the interface and the linker between the interface constituents, are important for ligase function. Although we do not observe autoinhibitory dimerization, the AS, as defined in studies using isolated HECT domain constructs, is indeed important for full activity of HUWE1.

Ubiquitin binding domains support ligase loading

In assessing HUWE1 activity compared with the HUWE1_{HECT} (Figure 1), we had observed not only near complete loss of Mcl1 and DDIT4 ubiquitination with HUWE1_{HECT} but also impaired ubiquitin loading of the ligase indicative of the N-terminal region of HUWE1 contributing to the catalytic activity of HUWE1. Ubiquitin binding domains in E3 ligases are thought to play a role in either substrate recognition or linkage specificity (Hurley et al., 2006; Kliza and Husnjak, 2020), and we hypothesized that the UB modules of HUWE1, which are flexibly tethered to the ring architecture, may critically contribute to ligase activity. We therefore introduced mutations that were reported to abolish binding to ubiquitin (Bomar et al., 2010; Tanno et al., 2014; Walinda et al., 2014) either alone or in combination, and assayed the resulting mutants in both the E2 discharge assay and the E3 ubiquitylation assay. We observe inhibition in our *in vitro* ubiquitylation assay (Figure S6B). In contrast to our expectations and the ascribed roles of ubiquitin binding domains, this inhibition seems to stem from an additive impairment of proper loading with ubiquitin or binding of the charged E2, as revealed in the E2 discharge assays (Figure S6C). These results shed a first light onto a possible role of the ubiquitin binding domains in the context of the full-length HUWE1 ligase. It should be noted that there are reported patient mutations implicated in ID located in the UB modules.

HUWE1 patient mutations are hypomorphic

Mapping patient mutations that lead to ID (Moortgat et al., 2018) onto the structure reveals four distinct classes (Figure S8). Class I comprises the mutations in the ubiquitin binding domain. Class II mutations lie in the vicinity of the ring-closure interface (Figure

5A); class III mutations map to the HECT domain, and class IV are distributed over ARLD1–3 but cluster in ARLD1. We chose representative mutations from classes II–IV, cloned and purified the corresponding proteins, and subjected them to E2 discharge and E3 ubiquitylation assays. Although the class II mutants (169–189, F3194S) show slightly decreased E2 discharge (Figure 5B), they show clear impairment of activity (Figure 5C). Interestingly, the class III mutant R4187C displays markedly increased E2 discharge (Figure 5B), while still being slightly impaired in E3 ligase activity (Figure 5C). The class IV mutation H669Q, which lies at the interface between the ring architecture and the HECT domain, shows no effect in overall E2 discharge or E3 activity and thus seems to be specific for a yet unknown (class of) substrate(s) (Figures 5B and 5C) and not generally modulatory of HUWE1 function. None of the tested mutations exhibits a complete loss of function, but rather all are hypomorphic to varying degrees, suggesting that even subtle perturbations of HUWE1 function can have drastic organismal consequences.

The observation that the region deleted in class II mutant 169–189 lies in the interface important for ring closure while retaining partial activity offers another opportunity to test the significance of this interface. If the closed ring represents a critical conformation in the HUWE1 catalytic cycle, the 169–189 deletion, while potentially shifting the open-to-closed ratio, should still be able to form a closed ring architecture. We therefore determined a structure of the 169–189 deletion allele of HUWE1 and find that this mutant still adopts the ring-shaped overall architecture, with an estimated ratio between open and closed conformation of about 2:1, which is comparable with wild-type (Figure S9). Despite the modest resolution (~4.5 Å) of the reconstruction, it becomes apparent how the ring interface is remodeled to accommodate the deleted 20 residues (Figure 5D). The interface forming loop (aa 3288–3299) moves upward toward the HECT domain, and the region directly following the deletion (aa 190–270) rearranges in the same direction to form a new interface. The fact that the hypomorphic 169–189 variant can form a closed ring, together with the observation that deliberately introduced interface mutations all had reduced activity, supports a model in which the closed conformation is important during the catalytic cycle of HUWE1. In summary, patient mutations in HUWE1 have a wide range of functional consequences, from those that seemingly do not influence overall activity, to those that mildly impair function, to those that largely ablate HUWE1 function. It is likely that these mutants also have different effects on different substrates or substrate classes, consistent with the various biological roles of this ligase.

Protein binding domains control substrate access and function

HUWE1 has at least two domains with substrate-selective features: (1) the WWE domain, implicated in directing HUWE1 toward PAR-modified (PARylated) substrates (Wang et al., 2012), facing the center of the solenoid (Figure S4J), and (2) the BH3 domain, which is known to recruit Mcl1 (Zhong et al., 2005). *In vitro* ubiquitylation assays confirmed that the BH3 domain is necessary for ubiquitylation of Mcl1 (Figure 6A). This observed requirement for the BH3 domain in Mcl1 ubiquitylation directly demonstrates that the difference in activity observed between HUWE1 and HUWE1_{HECT} (Figure 1B) is due, at least in part, to the absence of the substrate binding domain. As expected, mutations in the BH3 binding domain do not impair loading of the HECT domain with ubiquitin (Figure

S10A), which demonstrates that HUWE1 uses structurally distinct accessory domains that serve as integrated substrate receptors organized on a large scaffold. However, the handful of annotated functional domains within HUWE1 are outnumbered by the reported substrates of HUWE1, suggesting the existence of additional substrate-binding regions. We asked whether the ring architecture itself contributes to substrate binding, as the armadillo repeats that form ARLD1–4 are classical protein-protein interaction motifs that bind unfolded or extended peptides on their concave side (Mönkemeyer et al., 2019; Reichen et al., 2014). We thus set out to further characterize the interaction between HUWE1 and the model substrate DDIT4, which consists of a globular C-terminal region (aa 89–232) and an extended, disordered N-terminal stretch (aa 1–88). This N-terminal stretch of DDIT4 is dispensable for activity (Vega-Rubin-de-Celis et al., 2010), but its phosphorylation state has been linked to protein stability (Katiyar et al., 2009). Serendipitously, when we purify DDIT4 from insect cells, the protein splits into two populations during ion-exchange chromatography. The two populations correspond to different levels in phosphorylation (Figure S10B) of the N terminus, specifically in phosphorylation levels of residues Ser19, Thr23, and Thr25, as confirmed by mass spectrometry. Using both populations in an *in vitro* ubiquitylation assay with full-length HUWE1 reveals a preference of HUWE1 toward the phosphorylated species (Figure S10C). We hypothesized that these differences may result from a difference in binding and used a size exclusion chromatography (SEC) co-migration binding assay. Full-length HUWE1 was mixed with an excess of dephosphorylated and phosphorylated DDIT4, respectively. Western blot analysis of the peak fractions revealed increased binding of the phosphorylated species compared with the dephosphorylated species (Figures 6B and 6C).

On the basis of these findings, we collected a cryo-EM dataset of HUWE1 bound to phosphorylated DDIT4. The data were processed to ~3.3 Å overall resolution (Figure S11), revealing well-resolved density for HUWE1, essentially in the same conformation as the apo structure, with only the HECT domain in a slightly different orientation (Figure S11F). Consistent with an interaction involving the unstructured N-terminal part of DDIT4, no significant density for the C-terminal globular domain of DDIT4 was observed. Careful inspection of the map led us to identify two peptide-like stretches of density on the inside of the ring architecture that were absent in the reconstructions of apo HUWE. The first was found in a largely hydrophobic groove in the ARLD2 domain (Figures 6D and S12A–S12C). Our best efforts to assign a sequence to the density in the ARLD2 domain led us to tentatively build residues 3–9 (SLWDRFS) of DDIT4 (Figures S11G, S11H, and S12C). In this model, Leu4, Trp5, Arg7, and Phe8 would wedge into a crevice formed by parts of three ARLD2 helices (aa 939–954, aa 1051–1066, and aa 1123–1142). The large aromatic residues within the N terminus of DDIT4 are deeply buried within HUWE1, tightly held by residues Tyr941, Leu952, Ser1057, Arg1061, Ile1132, and Cys1133 of ARLD2 (Figure S12C). We repeated our SEC binding assay with a DDIT4 construct lacking the eight N-terminal residues (aa 9–232) and indeed saw further diminished binding compared with the DDIT4 wild-type (Figures 6B and 6C). DDIT4 ubiquitylation assays using these mutants did not show a significant difference, suggesting that the small differences in affinity are outside of the sensitivity of these *in vitro* assays and likely manifest only in a cellular context. The second peptide-like density is in a highly positively charged pocket of ARLD1

(Figures 6E and S12D-S12F), formed by Lys143, Arg144, Tyr391, His392, Arg431, and Arg434 of HUWE1 (Figure S12F). We could imagine a phospho-peptide corresponding to the phosphorylated N terminus occupying this pocket, but the quality of the reconstructed density does not allow sequence assignment with any level of confidence (Figure S12F).

To test if N-terminal sequence elements within DDIT4 are required for HUWE1-mediated degradation in human cells, we transiently transfected plasmids expressing GFP-tagged wild-type DDIT4, or versions without the N-terminal 8 (DDIT4- 8) or 88 (DDIT4- 88) amino acids. We observed that expression of both DDIT4- 8 and DDIT4- 88 resulted in elevated protein levels relative to wild-type DDIT4 (Figure S12G). These data suggest that removal of the N terminus of DDIT4 prevents efficient degradation in human cells, which is consistent with the observation that the N terminus is critical for binding to HUWE1 (Figure 6C). To examine if DDIT4 N-terminal truncation variants remain HUWE1 targets in a cellular context, we repeated the transient transfections of the DDIT4 variants in cells with doxycycline-inducible expression of a short hairpin RNA (shRNA) targeting HUWE1. Wild-type DDIT4 and DDIT4- 8 were stabilized upon HUWE1 knockdown. DDIT4- 88 protein levels, however, did not increase (Figure S12H). To confirm that the first 88 amino acids of DDIT4 were needed for HUWE1-mediated turnover, we expressed wild-type or catalytically inactive HUWE1 in cells with shRNA-mediated depletion of endogenous HUWE1. The exogenous versions of HUWE1 contain silent mutations that escape shRNA-mediated repression. Restoration of wild-type, but not catalytically inactive, HUWE1 expression reduced the levels of wild-type and DDIT4- 8 (Figure 6F). In contrast, DDIT4- 88 expression levels were unaffected by reintroducing wild-type HUWE1 (Figure 6F). Thus, HUWE1-mediated degradation of DDIT4 requires sequence elements within the N-terminal 88 amino acids of DDIT4.

DISCUSSION

HUWE1 has long been an enigmatic ligase implicated in many key cellular processes by ubiquitylating a wide array of substrates. In the absence of structures or biochemical dissections of the full-length ligase, the molecular basis for these diverse activities of HUWE1 has remained largely elusive. Our structural and functional characterization of HUWE1, the first of a full-length HECT ligase, reveals a ring-shaped modular architecture and demonstrates how multi-component proteins are more than just the sum of their parts (Figure 7A). One HUWE1 conundrum revolves around its ability to engage with such a large number of substrates. Dedicated binding domains, such as the BH3 and the WWE domain, allow binding of Mcl-1 and PARylated substrates (Figures 7B and 7C). Our structures establish an additional extended protein-protein interaction interface on the inner side of the ring. And although the DDIT4-bound structure does not allow unambiguous assignment of the density observed within the armadillo repeats, it supports a model in which HUWE1, in addition to the canonical protein binding modules, uses potentially degenerate peptide binding sites on the helical repeats to access or stabilize its substrates (Figure 7D). It is conceivable that multiple binding sites for the same target may exist and that the distinct substrate receptor domains cooperate with the helical repeats, allowing fine-tuning of substrate recruitment and ubiquitylation activity. It appears plausible that HUWE1 recruits many of its substrates through a series of low-affinity degenerate interactions.

Disordered peptide stretches, as well as sites for post-translational modifications (such as ubiquitylation, phosphorylation, and PARylation), are observed in many of the reported HUWE1 targets (Kao et al., 2018; Xu et al., 2016), and the described interactions of HUWE1 with phosphorylated DDIT4 may serve as a blueprint for the recognition of other substrates.

In addition to the helical repeats, the large disordered region (aa 2259–3179), which is mostly absent in the closest HUWE1 homolog in *S. cerevisiae* (Marín, 2018) (TOM1), may also contribute to binding a specific subset of substrates. The modularity observed in the structural data and evolution of HUWE1 (Giles and Grill, 2020; Grau-Bové et al., 2013; Marín, 2010, 2018) adapts well to its function as a major cellular rheostat that plays an important role in protein quality control and the destabilization of key regulators of cell growth and death. On the basis of our structure, it will now be possible to interrogate the binding modes of a diverse set of substrates in future studies.

The occurrence of both micro-duplications and missense mutations in patients suggests that both increased (gain of function) and decreased activity of HUWE1 (loss of function) can result in ID (Froyen et al., 2008; Giles and Grill, 2020; Moortgat et al., 2018). In this study, we find that all mutations we tested are either inactivating or benign. None of the patient mutations tested led to a complete loss of activity, in line with the essential role of HUWE1 and the observation that complete loss of HUWE1 is likely not tolerated in humans (Lek et al., 2016).

Although our study provides an important first view of a fully assembled HECT ligase, and the first mechanistic understanding of how the N-terminal ~3,900 amino acids of HUWE1 cooperate with its catalytic HECT domain in the regulation of diverse substrates, key questions remain to be addressed. For example, it remains to be shown what exact roles the open and the closed conformation of HUWE1 play throughout the ubiquitylation cycle (Figure 7D). All of our results point toward the fact that the closed ring architecture is important, as ring-interface mutations inhibit both E2 discharge and E3 activity. Whether it is necessary for HUWE1 to sample the open conformation at some point during the ubiquitylation cycle remains hypothetical yet plausible, as an open conformation supported by the highly flexible nature of the ring architecture and the HECT domain would allow to establish a large “ubiquitination zone.” Future studies might try to tackle this question by using protein engineering to trap HUWE1 in one or the other conformation.

The mechanistic understanding of substrate recruitment and regulation provided here will facilitate the further elucidation of the complex role HUWE1 plays in regulating cellular stress responses (Costa-Mattioli and Walter, 2020). Moreover, as HUWE1 has recently been demonstrated to be a key sensitizer to commonly used anti-cancer agents (Olivieri et al., 2020), our structure may suggest routes to new therapeutics that shift the apoptotic threshold. In particular, it may inform the design of substrate-selective recruiting or inhibiting small molecules.

Limitations of the study

A major question not resolved by the present study relates to the significance of the “open” conformation observed in our cryo-EM studies. Although cryo-EM uses vitrification of samples in solution, physical forces, such as those at the air-water interface can lead to “broken” particles. However, it is also conceivable that the “open” conformation represents an important state of the catalytic cycle. Although mutations designed to weaken/break the interface led to reduced activity, consistent with the “closed” conformation being important for activity, mutations designed to strengthen the interface did not show any significant effect, which unfortunately could be due to either the open conformation being non-physiological or the mutations being benign and therefore inconclusive. Additional studies such as single-molecule techniques may be able to shed light on this in future studies. We also point out that the density observed for DDIT4 is not unambiguous, and although together with biochemical and cellular characterization clearly supporting the utility of the ring in binding peptides does not explain the precise molecular interactions that constitute the DDIT4-HUWE1 ligase-substrate relationship. Unstructured regions in proteins are often required as initiation sites for degradation by the proteasome (Prakash et al., 2004), and we would like to point out that the increased cellular stabilization observed upon removing the N terminus of DDIT4 could also be in part due to removal of the degradation initiation site.

STAR★METHODS

RESOURCE AVAILABILITY

Lead contact—Further information and requests for resources and reagents should be directed to and will be fulfilled by the lead contact, Eric Fischer (eric_fischer@dfci.harvard.edu).

Materials availability—Reagents generated in this study are available from the lead contact with a completed Materials Transfer Agreement.

Data and code availability—Cryo-EM maps and models have been deposited in the EMDB and PDB, respectively, under accession codes EMDB: EMD-22427 (BS3-crosslinked, consensus, PDB: 7JQ9), EMDB: EMD-22428 (BS3-crosslinked, focus on HECT, PDB: 7MWD), EMDB: EMD-22429 (BS3-crosslinked, focus on WWE, PDB: 7MWE), EMDB: EMD-22430 (BS3-crosslinked, focus on interface, PDB: 7MWF), EMDB: EMD-22431 (non-crosslinked), EMDB: EMD-23931 (HUWE1 169-189), and EMDB: EMD-23925 (HUWE1-DDIT4 complex, PDB: 7MOP). Data are available upon time of publication. Uncropped gels and western blot source data have been deposited to Mendeley Data: <https://dx.doi.org/10.17632/zj4thx3b4b.1> and are publicly available as of the date of publication.

This paper does not report original code.

Any additional information required to reanalyze the data reported in this paper is available from the lead contact upon request.

EXPERIMENTAL MODEL AND SUBJECT DETAILS

All protein mutants used in this study were cloned as described in the Method details, and isolated from NEB10b *E. coli* cells grown at 37°C in LB medium.

All strains and cell lines used in this study for virus production, recombinant protein expression and cellular assays are listed in the Key resources table. Sf9 and Hi5 cells were maintained in ESF921 and SF-900 medium, respectively, at 27°C. Expi293F cells were maintained in Expi293 medium at 37°C and 8% CO₂. All cell lines are routinely tested for mycoplasma contamination with LookOut and MycoAlert Mycoplasma detection kits. 293T cells were grown in DMEM supplemented with 10% FBS at 37°C and 5% CO₂. Commercial cell lines were not authenticated.

METHOD DETAILS

Cloning, protein expression and purification—A HUWE1 Entry clone (pENTR1A-HUWE1 was a gift from Jean Cook (Addgene plasmid #37431)) was re-cloned to represent canonical isoform 1 sequence using standard restriction/ligation cloning (amino acids (aa) 1-4374, UniProt: Q7Z6Z7). For cellular assays, the coding sequence was hardened against doxycycline-inducible shRNA by introducing silent DNA mutations within every codon of HUWE1 recognized by the shRNA. HUWE1 mutant sequences were generated by excising pieces from this Entry clone using unique restriction sites, followed by insertion of synthesized double-stranded DNA (gBlocks, IDT) carrying desired mutations using Gibson assembly (New England Biolabs). Modified pDEST plasmid (Thermo Fisher Scientific) and pDARMO (pDarmo.CMVT_v1 was a gift from David Sabatini [Addgene plasmid #133072]) plasmids were used to transiently express wild-type full-length HUWE1 and all mutants described in this study carrying either an N-terminal 1xFLAG-tag or 3xFLAG-tag in Expi293 cells (Thermo Fisher Scientific) following the manufacturer's manual (Figures S1A, S1F, and S1G). Cells were harvested 48-60 hours post transfection and lysed by sonication in lysis buffer (50 mM HEPES/KOH pH 7.4, 200 mM NaCl, 2 mM MgCl₂, 5% glycerol) supplemented with protease inhibitors. The lysate was cleared by ultracentrifugation (45 min, 120,000 g) and incubated with FLAG-antibody-coated beads for 1 hour at 4°C. Beads were washed with lysis buffer and protein was eluted with 5 column volumes of lysis buffer supplemented with 0.15 mg/ml 1xFLAG (DYKDDDDK) or 3xFLAG (MDYKDHDGDYKDHDIDYKDDDDK) peptide. The protein was concentrated using centrifugal concentrators (Amicon, 30 kDa molecular weight cut-off (MWCO)) and polished by size exclusion chromatography (SEC, Superose 6 Increase, GE Healthcare) in gel filtration buffer (30 mM HEPES/KOH pH 7.4, 150 mM NaCl, 2 mM TCEP). For size exclusion co-migration assay, HUWE1 was expressed and purified from a modified pDARMO plasmid using a C-terminal 3xFLAG tag, following the same purification procedure.

Coding sequences of full-length and mutant DDIT4 (Harvard plasmid repository, HsCD00327445, a 1-232, UniProt: Q9NX09), MCL1- TM (HsCD00004569, amino acid residues 1-327, UniProt: Q07820) and HUWE1_{HECT} (aa 3993-4374) were subcloned into pAC8-derived vectors (Abdulrahman et al., 2009) and baculovirus was generated in *Spodoptera frugiperda* Sf9 cells grown in ESF921 medium (Expression Systems) following

the manufacturer's manual. Large-scale expression of Strep-tagged proteins for purification was conducted in *Trichoplusia Ni* High Five cells (Thermo Fisher Scientific) in SF-900 medium (GIBCO). Cells at a density of 2×10^6 cells/ml were infected with 1.5% of amplified virus and incubated for 40 hours. After harvest, cells were lysed by sonication in lysis buffer and the lysate was cleared by ultracentrifugation (45 min, 120,000 g). The supernatant was bound to StrepTactin XT High Capacity resin (IBA) in a gravity flow column. The resin was washed with lysis buffer and the proteins were eluted with lysis buffer supplemented with 50 mM biotin. For DDIT4 and Mcl1 constructs, the salt concentration was brought to 50 mM by addition of dilution buffer (50 mM HEPES/KOH pH 7.4, 2 mM TCEP) and proteins were further purified by ion exchange chromatography using a Poros 50HQ (Thermo Fisher Scientific) column, eluting with a linear NaCl-gradient from 50 mM to 750 mM. Protein-containing fractions were combined, concentrated using centrifugal concentrators (Amicon, 10 kDa MWCO), and final polishing was performed by SEC (Superdex200, GE Healthcare) in a buffer containing 30 mM HEPES/KOH pH 7.4, 200 mM NaCl, 2 mM TCEP. During ion exchange chromatography, DDIT4 split into two species (DDIT4_peak1, and DDIT4_peak2) depending on phosphorylation state of amino acids Ser19, Thr23 and Thr25, as confirmed by mass spectrometry. For dephosphorylation, DDIT4 species were treated with λ -protein phosphatase (NEB,) according to manufacturer's manual.

***In vitro* ubiquitylation assays**—*In vitro* ubiquitylation reactions were carried out in a total volume of 15 μ l with UBE1 at 0.2 μ M (R&D Systems), UbcH5b at 0.5 μ M (R&D Systems), Mg-ATP (R&D Systems) at 10 mM, ubiquitin at 50 μ M (R&D Systems), buffered with 1X E3 Ligase Reaction Buffer (R&D Systems). Reactions were pre-incubated for 30 minutes to allow charging of the E2 and then initiated by addition of wild-type or mutant HUWE1 at 0.21 μ M and Strep-tagged substrate (DDIT4_peak 2, Mcl1) at 2 μ M, and were allowed to react for the indicated reaction time at room temperature. Reaction products were analyzed by SDS-PAGE and subsequent immunoblotting with an anti-Mcl1 rabbit antibody (1:1,000) for Mcl1 and anti-Strep antibody HRP conjugate (1:16,000) for DDIT4, respectively. Anti-Mcl1 blots were imaged using a LI-COR CLx detecting an anti-rabbit secondary antibody (IRDye800CW Donkey anti-rabbit), and anti-Strep blots were imaged using an Amersham Imager 600 and Amersham ECL Prime Western Blotting Detection Reagent (GE Life Sciences).

Single-turnover E2 discharge assay—The E2 discharge assay to monitor ubiquitin (Ub) transfer from E2 to HUWE1 was performed in two steps. First, UbcH5B at 9.1 μ M (R&D Systems) was reacted with UBE1 at 0.42 μ M (R&D Systems) and fluorescent Ub at 16.7 μ M (R&D Systems) buffered in 50 mM Tris 7.6, 300 mM NaCl. This reaction was initiated with 2 mM Mg-ATP (R&D Systems) for 30 min at room temperature and then quenched by diluting four-fold with 25 mM HEPES 7.5, 100 mM NaCl, 25 mM EDTA. The pre-charged E2-Ub mixture was mixed with excess wild-type or mutant HUWE1 at room temperature in a total reaction volume of 15 μ l with 0.08 μ M of E2-Ub and 0.4 μ M HUWE1. At the indicated reaction times, the reactions were quenched with 4x SDS sample loading buffer lacking reducing agent. Reaction mixtures were separated by SDS-PAGE and gels were analyzed by fluorescent imaging on a Typhoon FLA 9500 (GE Life Sciences). Intensities of the bands were quantified by ImageJ and normalized to the

E2-Ub only control. Error bars signify standard deviation and are generated from triplicate measurements. All plots were generated with prism 7.0.

EM sample preparation and data collection—For dataset 1 (BS3-crosslinked), HUWE1 eluted from affinity resin was buffer-exchanged using Zeba Spin Desalting Columns (Thermo Fisher Scientific) and incubated with 1.5 mM bis(sulfosuccinimidyl)suberate (BS3, Thermo Fisher Scientific) at room temperature for 20 minutes. Samples were quenched with 100 mM Tris pH 7 before the final SEC step. CHAPSO (Hampton Research) at 0.8 mM was added to HUWE1 at concentrations of 0.9 mg/ml directly before grid preparation. Glow-discharged Quantifoil 1.2/1.3 grids were prepared using a Leica EM-GP, operated at 10°C and 95% relative humidity. 4 μ l samples were applied twice and blotted for 2.25 s each time. Grids were imaged in an Titan Krios equipped with a Gatan Quantum Image filter (20 eV slit width) and a post-GIF Gatan K3 direct electron detector. Images were acquired at 300 kV at a nominal magnification of 105,000 x in counting mode with a pixel size of 0.85 Å/pixel using SerialEM (Schorb et al., 2019). Three movies (40 frames each) were acquired per hole with four holes per stage position (resulting in 12 image acquisition groups), in a defocus range from -0.8 - -2.5 μ m over an exposure time of 2.4 s and a total dose of 45.68 $e^-/\text{Å}^2$.

For dataset 2 (non-crosslinked), an additional purification step was included between affinity purification and polishing. After elution from FLAG antibody-coated beads, the sample was diluted with dilution buffer to lower the salt concentration (50 mM HEPES/KOH pH 7.4, 2 mM TCEP) and subjected to ion exchange chromatography (Poros 50HQ, Thermo Fisher Scientific), eluted with a linear NaCl-gradient from 50 mM to 750 mM. Peak fractions were pooled, concentrated using centrifugal concentrators (Amicon, 30 kDa MWCO) and polished by SEC. CHAPSO at a concentration of 0.8 mM was added to 0.4 mg/ml HUWE1 directly before grid preparation. 4 μ l sample was applied to glow-discharged Quantifoil 1.2/1.3 grids and the grids were vitrified using a Leica EM-GP (3 s blotting), operated at 10°C and 95% relative humidity. Grids were imaged in an Titan Krios equipped with a Gatan Quantum Image filter (20 eV slit width) and a post-GIF Gatan K2 direct electron detector. Images were acquired using SerialEM at 300 kV at a nominal magnification of 130,000 x in super-resolution mode with a pixel size of 0.53 Å per super-resolution pixel at the specimen level. Three movies (35 frames each) were acquired per hole with four holes per stage position (resulting in 12 image acquisition groups), in a defocus range from -1 - -2.3 μ m over an exposure time of 7 s and a total dose of 49.37 $e^-/\text{Å}^2$.

For dataset 3 (169-189 mutant), HUWE1 mutant was purified as wild-type HUWE1 used for dataset 1, but omitting the crosslinking reaction. CHAPSO (Hampton Research) at 1 mM was added to HUWE1 at concentrations of 1.8 mg/ml directly before grid preparation. Glow-discharged Quantifoil 1.2/1.3 grids were prepared using a Leica EM-GP, operated at 10°C and 90% relative humidity. 4 μ l samples were applied and blotted for 3.5 s. Grids were imaged in an Talos Arctica equipped Gatan K3 direct electron detector. Images were acquired at 200 kV at a nominal magnification of 36,000 x in counting mode with a pixel size of 1.13 Å/pixel using SerialEM. Movies (50 frames each) were acquired in a defocus range from -1 - -2.2 μ m over an exposure time of 6 s and a total dose of 54.86 $e^-/\text{Å}^2$.

For dataset 4 (HUWE1-DDIT4 complex), HUWE1 (after affinity purification step) was mixed with a 3x molar excess of purified DDIT4_peak2, incubated at room temperature for 30 minutes and passed over a Superose 6 size exclusion column. Peak fractions were pooled, concentrated using centrifugal concentrators (Amicon, 10 kDa MWCO), and 1 mM CHAPSO was added to 1.5 mg/ml HUWE1 directly before grid preparation. 4 μ l samples were applied twice onto glow-discharged Quantifoil 1.2/1.3 grids, blotted for 3.25 s each time, and vitrified in a Leica EM-GP, operated at 10°C and 95% relative humidity. Grids were imaged in an Titan Krios equipped with a Gatan Quantum Image filter (20 eV slit width) and a post-GIF Gatan K3 direct electron detector. Images were acquired with SerialEM at 300 kV at a nominal magnification of 105,000 x in counting mode with a pixel size of 0.825 Å/pixel. Two movies (50 frames each) were acquired per hole with four holes per stage position (resulting in 8 image acquisition groups), in a defocus range from -0.8 - -2.5 over an exposure time of 2.5 s and a total dose of 53.34 e⁻/Å².

Data processing and model building—Dataset 1 (BS3-crosslinked): 10,390 movies were corrected for beam-induced motion using UCSF MotionCor2 (Zheng et al., 2017) (v1.2.1) and contrast transfer function (CTF) was estimated using CTFFIND4.1 (Rohou and Grigorieff, 2015) (v4.1.10). Poor quality micrographs (CTF resolution estimation > 4.9 Å) and micrographs with apparent ice contamination were discarded. 2,110,785 particles were picked from the 9610 remaining micrographs using crYOLO (Wagner et al., 2019) (v1.2.2) trained on a subset of manually picked particles. Particles were extracted with a box size of 364 pixels (309.5 Å) and down-sampled by Fourier-cropping to a box size of 224 pixels with 1.38 Å/pix in Relion-3.0 (Scheres, 2012; Zivanov et al., 2018) (v3.0-beta-2). Particles were cleaned through several rounds of reference-free 2D classification in cryoSPARC (Punjani et al., 2017) (v2.4.6, unless otherwise noted), and an initial model was calculated from 1,262,934 particles. The particle set (re-extracted with the original pixel size) and resulting initial model were used to further clean up the dataset using 3D classification in Relion-3.0. The remaining 762,898 particles went through two rounds of CTF-Refinement and Bayesian polishing implemented in Relion-3.0, globally refining CTF parameters in the first round, followed by CTF-Refinement per image acquisition group in the second round. A consensus refinement yielded a map at 3.3 Å resolution. Masked classification was used to identify subsets of particles with better defined features (Figure S2) for the HECT domain (33,078 particles used for reconstruction, 3.8 Å), the WWE/AB/Tower region (85,184 particles, 3.6 Å,) and the N terminus and interface region (125,477 particles, 3.4 Å.). Available crystal structures of the HECT domain (PDB: 5LP8 (Sander et al., 2017)) and the WWE domain (PDB: 6MIW) could readily be rigid body-fitted into the maps (Figures S4G and S4I), and all maps were used for manual model building in COOT (Emsley et al., 2010) (v0.9-pre). Density for the two N-terminal helices (aa 17-27 and aa 31-39) was very weak and did not allow building with high confidence. Two idealized helices based on secondary structure prediction were placed and fitted as rigid bodies into the density. A refined detector pixel size was later determined to be 0.825 Å/pix, so the particle dataset after the first round of Bayesian polishing was imported into Relion-3.1 (Zivanov et al., 2020) (v3.1-beta) for reprocessing. In short, beam tilt and anisotropic magnification were refined per image acquisition group. 4th order aberration estimation was used to refine spherical aberration and to estimate the error in the CTF estimation which

resulted from using the wrong nominal pixel size in initial processing steps. Refinements resulting in the four maps that were used for model building were repeated, and the resulting maps were re-scaled to a pixel size of 0.825 Å/pix during PostProcess. These final maps (Figure S2) were deposited as main maps (3.1 Å, EMDB: EMD-22427; 3.7 Å, EMDB: EMD-22428; 3.4 Å, EMDB: EMD-22429; 3.3 Å, EMDB: EMD-22430). The model was protonated (phenix.-reduce) and different parts were individually refined in the maps where they were best resolved (aa 3953-4364 in EMDB: EMD-22428, aa 1595-2109 and 2512-2696 in EMDB: EMD-22429, aa 17-376 and aa 3179-4005 in EMDB: EMD-22430, aa 377-1594 and aa 2109-2259 in EMDB: EMD-22427). For this, density around the respective part was cut out (using phenix.cut_out_densities (Adams et al., 2010; Afonine et al., 2018) (v1.17.1)) and used for iterative refinement of the atomic model with ISOLDE (Croll, 2018) (v1.0b4) and phenix.real_space_refine, using adp and rigid body refinement, gradient-driven minimization and simulated annealing. The high-resolution crystal structures of the WWE and the HECT domain as well as the ISOLDE-refined model for the helical repeats were used as target restraints. Finally, the combined model was refined with target restraints against all deposited maps (PDBs: 7JQ9, 7MWD, 7MWE, 7MWF). Data collection parameters and final refinement statistics are available as Table S1, a list of all deposited maps from this dataset is available as Table S2.

Dataset 2 (non-crosslinked): 9,225 movies were corrected for beam-induced motion and Fourier-cropped by a factor of 2 (resulting in a pixel size of 1.06 Å/pix) using the Relion-3.0 MotionCor implementation, and CTF was estimated using CTFFIND4.1 (v4.1.10). Poor quality micrographs (CTF resolution estimation > 5.9 Å) and micrographs with apparent ice contamination were discarded. 2,902,388 particles were picked from the 8404 remaining micrographs by crYOLO (v1.2.2) using the model from dataset 1. Particles were extracted with a box size of 288 pixels (305.3 Å) and down-sampled to a box size of 200 pixels with 1.52 Å/pix in Relion-3.0. Particles were cleaned through several rounds of reference-free 2D classification in cryoSPARC, and four initial *ab initio* models were calculated from 1,356,068 particles. 3 classes represented an open form of HUWE1, and one class represented the closed form observed in dataset 1. The increased flexibility of this open form precluded high-quality 3D reconstructions (Video S1). Particles in the class representing the closed conformation (~27%) were further cleaned from low-quality particles by calculating 6 additional *ab initio* models. Good particles (336,853) were re-extracted in Relion-3.0 to the original pixel size, defocus values were estimated per particle in CtfRefine, followed by Bayesian polishing. The resulting particles with enhanced signal were imported back into cryoSPARC for final non-uniform refinement (Punjani et al., 2020), yielding a map at 3.4 Å (EMDB: EMD-22431; Figure S5). A correlation of 0.94 between final maps from dataset 1 and dataset 2 at comparable levels (0.0146 and 0.52, respectively) was determined in Chimera (Pettersen et al., 2004). Data collection parameters are available in Table S1, a list of all deposited maps from this dataset is available as Table S2.

Dataset 3 (HUWE1 169-189): 3,862 movies were corrected for beam-induced motion using UCSF MotionCor2 (v1.2.1), CTF was estimated using CTFFIND4.1 (v4.1.10), and movies with a resolution estimation worse than 6.5 Å were discarded (3,821 movies remained). 992,194 particles were picked with crYOLO (v1.2.2), using an updated model from dataset 1 and extracted with a box size of 278 pixels (~311 Å) and resampled to a box

size of 180 pixels (1.75 Å/pixel). The dataset was cleaned using 2D and 3D classification in Relion-3.1. The resulting 60,560 particles went through CTF-Refinement and Bayesian polishing, resulting in a polished particle set yielding a reconstruction at 4.5 Å (Figure S9; EMDB: EMD-23931). Data collection parameters are available in Table S1, a list of all deposited maps from this dataset is available as Table S2.

Dataset 4 (HUWE1-DDIT4 complex): 7,208 movies were corrected for beam-induced motion using UCSF MotionCor2 (v1.2.1) and CTF was estimated using CTFFIND4.1 (v4.1.10). 1,673,531 particles were picked with crYOLO (v1.2.2), using an updated model from dataset 1. Particles were extracted with a box size of 364 pixels (300.3 Å) and down-sampled to a box size of 224 pixels with 1.34 Å/pix in Relion-3.1. The dataset was cleaned up from non-particle picks through two rounds of 2D classification in cryoSPARC2 (v2.12.4). 558,215 particles were used for *ab initio* reconstruction and heterogeneous refinement of 3 initial volumes to remove open HUWE1 particles (~30%), and particles (378,785) from good classes representing closed HUWE1 were re-extracted with the original pixel size into Relion-3.1. Dataset was further polished through 4 rounds of 3D classification and one round of 2D classification. Beam tilt, 3-fold astigmatism and 4th order aberrations were estimated per acquisition group for particles belonging to the best resulting classes (312,798), followed by Bayesian polishing. After an additional round of 2D classification, a consensus refinement yielded a map at 3.3 Å resolution (Figure S11; EMDB: EMD-23925). The HUWE1 model determined from dataset 1 could readily be docked, the orientation of the HECT domain was adjusted by rigid body fit in a low-pass filtered map (Figure S11F). The DDIT4 peptide stretch was built manually in COOT. The resulting model was refined against the map using phenix.real_space_refine, as described above (PDB: 7MOP). Data collection parameters and refinement statistics are available in Table S1, a list of all deposited maps from this dataset is available as Table S2.

The resolutions of all maps are given based on the Fourier shell correlation (FSC) 0.143 threshold criterion (Rosenthal and Henderson, 2003; Scheres and Chen, 2012). Map and model resolution ranges were judged by local resolution histograms (Figures S3C, S3F, S3I, S3L, S5E, S9E, and S11E). Maps sharpened with automatically determined B-values (from Relion-3.1 or cryoSPARC) were deposited as main maps in the EMDB, and all maps that were used for figure preparations blurred to different B-values or post-processed with deepEMhancer (Sanchez-Garcia et al., 2020) were deposited as additional maps under the corresponding EMDB identifier (see Table S2).

Interface areas were calculated using PDBePisa (Krissinel and Henrick, 2007), and figures of models and EM maps were generated using ChimeraX (Goddard et al., 2018) and Chimera. 3D structural variability movies (Punjani and Fleet, 2021) were visualized with Chimera. Structural similarity searches were conducted using PDBeFold (Krissinel and Henrick, 2004), using standard 70% thresholds for both query and target for ARLD1, ARLD3 and ARLD4, while the thresholds were lowered to 40% and 50% for query and target, respectively, for ARLD2. For ARLD1, ARLD2 and ARLD4, armadillo repeat-like proteins populated the top hits. For ARLD3 top hits included ENTH-domain proteins, which are also reminiscent of armadillo repeats (Legendre-Guillemain et al., 2004). Structural

biology applications used in this project were compiled and configured by SBGrid (Morin et al., 2013).

Size exclusion co-migration assay—~380 µg HUWE1 with C-terminal 3xFLAG tag were mixed with 3-fold molar excesses of N-terminally Strep-tagged DDIT4 variants, incubated for 1 hour at room temperature and applied to a Superose 6 Increase 10/300 (GE Healthcare). Peak fractions were analyzed by SDS-PAGE and subsequent immunoblotting with anti-Strep antibody HRP conjugate (1:60,000) and anti-FLAG M2 antibody (1:4,000), respectively. Anti-Strep blots were imaged using an Amersham Imager 600 and Amersham ECL Prime Western Blotting Detection Reagent (GE Life Sciences). Anti-FLAG blots were imaged using LI-COR CLx detecting an anti-mouse secondary antibody (IRDye680 Goat-Anti mouse).

Cellular protein stability assays—Plasmids to express full-length HUWE1 and DDIT4 in human cells were generated by Gateway cloning into CMV driven N-terminal FLAG- or GFP-tagged expression vectors. 293T cells were grown in DMEM supplemented with 10% FBS and penicillin/streptomycin at 37°C with 5% CO₂. The plasmid containing doxycycline-inducible shRNA targeting HUWE1 was obtained from Dharmacon (TRIPZ_HUWE1_shRNA_V3THS_353155) and introduced into 293T cells by lentiviral transduction. A stable population was selected and maintained by culturing the cells with 1 µg/mL Puromycin. Expression of the shRNA was induced by the addition of 2 µg/mL doxycycline, with media changes and fresh doxycycline added every 24 hours. Transient transfections were performed using Lipofectamine 2000 (Thermo Fisher). Cells were harvested for analysis 48 hours after transfection. For immunoblot analysis, cell pellets were resuspended in urea lysis buffer (8M urea, 50mM Tris pH 8, 75mM NaCl, 1mM NaV, 1mM NaF, 1mM β-glycerophosphate, 40mM NEM, Roche EDTA-free protease inhibitor cocktail). Cells were lysed by sonication and cleared by centrifugation. Lysate protein concentrations were measured by BCA Protein Assay (Thermo Fisher) and equal amounts of protein were mixed with Laemmli sample buffer with β-mercaptoethanol and loaded onto 6% (for HUWE1 immunoblotting) or 15% (for GFP and tubulin immunoblotting) SDS-PAGE gels. Gels were semi-dry transferred to PVDF using the Bio-Rad Turbo Transfer system for 30 min at 25V. Immunoblots were blocked with 4% milk in TBST. Primary antibodies were diluted in 5% BSA in TBST (anti-HUWE1 and anti-GFP antibodies diluted 1:1,000, anti-tubulin antibody diluted 1:5,000). HRP-conjugated secondary antibodies were diluted 1:10,000 in 4% milk in TBST. Immunoblots were developed using Clarity (BioRad) and imaged with a Chemi-Doc XRS+ (Bio-Rad).

QUANTIFICATION AND STATISTICAL ANALYSIS

No quantification was performed for western blot-based ubiquitylation assays described in ‘*In vitro* ubiquitylation assays’, all reactions were repeated at least three times. For E2 discharge assays described in ‘Single-turnover E2 discharge assay’, band intensities were quantified and normalized to a control band on the same gel using ImageJ. For statistical analysis, three independently pipetted experiments were considered, and the standard deviation is presented using error bars. At least three biological replicates were performed

for each cellular assay. Representative western blots are shown, and no quantification was performed.

Supplementary Material

Refer to Web version on PubMed Central for supplementary material.

ACKNOWLEDGMENTS

This work was supported by NIH grants National Cancer Institute (NCI) R01CA2144608 and U54CA231637 to E.S.F. and R01GM127681 to E.J.B. E.S.F. is a Damon Runyon-Rachleff Investigator (DRR-50-18). J.K.M. was supported by a postdoctoral fellowship (PF-19-072-01 – TBE) from the American Cancer Society. M.H. was supported by Swiss National Science Foundation (Switzerland) fellowships 174331 and 191053. M.W.M. was supported in part by the Chleck Foundation. We thank the staff at the University of Massachusetts Medical School Cryo-EM Core Facility and the Harvard Cryo-EM Center for Structural Biology for their support during grid screening and data collection. We acknowledge the SBGrid consortium for assistance with high-performance computing. We also thank Michael J. Eck, Nicolas H. Thomä, Nathanael S. Gray, Stephen C. Harrison, and Johannes C. Walter for critical feedback on the manuscript.

REFERENCES

- Abdulahman W, Uhring M, Kolb-Cheynel I, Garnier JM, Moras D, Rochel N, Busso D, and Poterszman A (2009). A set of baculovirus transfer vectors for screening of affinity tags and parallel expression strategies. *Anal. Biochem* 385, 383–385. [PubMed: 19061853]
- Adams PD, Afonine PV, Bunkóczi G, Chen VB, Davis IW, Echols N, Headd JJ, Hung LW, Kapral GJ, Grosse-Kunstleve RW, et al. (2010). PHENIX: a comprehensive Python-based system for macromolecular structure solution. *Acta Crystallogr. D Biol. Crystallogr* 66, 213–221. [PubMed: 20124702]
- Adhikary S, Marinoni F, Hock A, Hulleman E, Popov N, Beier R, Bernard S, Quarto M, Capra M, Goettig S, et al. (2005). The ubiquitin ligase HectH9 regulates transcriptional activation by Myc and is essential for tumor cell proliferation. *Cell* 123, 409–421. [PubMed: 16269333]
- Afonine PV, Poon BK, Read RJ, Sobolev OV, Terwilliger TC, Urzhumtsev A, and Adams PD (2018). Real-space refinement in PHENIX for cryo-EM and crystallography. *Acta Crystallogr. D Struct. Biol* 74, 531–544. [PubMed: 29872004]
- Amici DR, Jackson JM, Metz KA, Ansel DJ, Smith RS, Brockway S, Takagishi SR, Srivastava S, O'Hara BP, Cho B-K, et al. (2019). Coessential genetic networks reveal the organization and constituents of a dynamic cellular stress response. *bioRxiv*. 10.1101/847996.
- Bernassola F, Chillemi G, and Melino G (2019). HECT-type E3 ubiquitin ligases in cancer. *Trends Biochem. Sci* 44, 1057–1075. [PubMed: 31610939]
- Bomar MG, D'Souza S, Bienko M, Dikic I, Walker GC, and Zhou P (2010). Unconventional ubiquitin recognition by the ubiquitin-binding motif within the Y family DNA polymerases iota and Rev1. *Mol. Cell* 37, 408–417. [PubMed: 20159559]
- Bosshard M, Aprigliano R, Gattiker C, Palibrk V, Markkanen E, Backe PH, Pellegrino S, Raymond FL, Froyen G, Altmeyer M, et al. (2017). Impaired oxidative stress response characterizes HUWE1-promoted X-linked intellectual disability. *Sci. Rep* 7, 15050. [PubMed: 29118367]
- Brugarolas J, Lei K, Hurley RL, Manning BD, Reiling JH, Hafen E, Witters LA, Ellisen LW, and Kaelin WG Jr. (2004). Regulation of mTOR function in response to hypoxia by REDD1 and the TSC1/TSC2 tumor suppressor complex. *Genes Dev.* 18, 2893–2904. [PubMed: 15545625]
- Cassidy KB, Bang S, Kurokawa M, and Gerber SA (2020). Direct regulation of Chk1 protein stability by E3 ubiquitin ligase HUWE1. *FEBS J.* 287, 1985–1999. [PubMed: 31713291]
- Chen D, Kon N, Li M, Zhang W, Qin J, and Gu W (2005). ARF-BP1/Mule is a critical mediator of the ARF tumor suppressor. *Cell* 121, 1071–1083. [PubMed: 15989956]
- Clements KE, Hale A, Tolman NJ, Nicolae CM, Sharma A, Thakar T, Liang X, Kawasawa YI, Wang H-G, De S, et al. (2019). Identification of regulators of poly-ADP-ribose polymerase (PARP)

- inhibitor response through complementary CRISPR knockout and activation screens. *bioRxiv*. 10.1101/871970.
- Costa-Mattioli M, and Walter P (2020). The integrated stress response: from mechanism to disease. *Science* 368, eaat5314. [PubMed: 32327570]
- Croll TI (2018). ISOLDE: a physically realistic environment for model building into low-resolution electron-density maps. *Acta Crystallogr. D Struct. Biol* 74, 519–530. [PubMed: 29872003]
- Emsley P, Lohkamp B, Scott WG, and Cowtan K (2010). Features and development of Coot. *Acta Crystallogr. D Biol. Crystallogr* 66, 486–501. [PubMed: 20383002]
- Froyen G, Corbett M, Vandewalle J, Jarvela I, Lawrence O, Meldrum C, Bauters M, Govaerts K, Vandeleur L, Van Esch H, et al. (2008). Submicroscopic duplications of the hydroxysteroid dehydrogenase HSD17B10 and the E3 ubiquitin ligase HUWE1 are associated with mental retardation. *Am. J. Hum. Genet* 82, 432–443. [PubMed: 18252223]
- Giles AC, and Grill B (2020). Roles of the HUWE1 ubiquitin ligase in nervous system development, function and disease. *Neural Dev.* 15, 6. [PubMed: 32336296]
- Goddard TD, Huang CC, Meng EC, Pettersen EF, Couch GS, Morris JH, and Ferrin TE (2018). UCSF ChimeraX: meeting modern challenges in visualization and analysis. *Protein Sci.* 27, 14–25. [PubMed: 28710774]
- Grau-Bové X, Sebé-Pedrós A, and Ruiz-Trillo I (2013). A genomic survey of HECT ubiquitin ligases in eukaryotes reveals independent expansions of the HECT system in several lineages. *Genome Biol. Evol* 5, 833–847. [PubMed: 23563970]
- Hall JR, Kow E, Nevis KR, Lu CK, Luce KS, Zhong Q, and Cook JG (2007). Cdc6 stability is regulated by the Huwe1 ubiquitin ligase after DNA damage. *Mol. Biol. Cell* 18, 3340–3350. [PubMed: 17567951]
- Herold S, Hock A, Herkert B, Berns K, Mullenders J, Beijersbergen R, Bernards R, and Eilers M (2008). Miz1 and HectH9 regulate the stability of the checkpoint protein, TopBP1. *EMBO J.* 27, 2851–2861. [PubMed: 18923429]
- Hershko A, and Ciechanover A (1998). The ubiquitin system. *Annu. Rev. Biochem* 67, 425–479. [PubMed: 9759494]
- Hurley JH, Lee S, and Prag G (2006). Ubiquitin-binding domains. *Biochem. J* 399, 361–372. [PubMed: 17034365]
- Kamadurai HB, Souphron J, Scott DC, Duda DM, Miller DJ, Stringer D, Piper RC, and Schulman BA (2009). Insights into ubiquitin transfer cascades from a structure of a UbcH5B approximately ubiquitin-HECT(NEDD4L) complex. *Mol. Cell* 36, 1095–1102. [PubMed: 20064473]
- Kamadurai HB, Qiu Y, Deng A, Harrison JS, Macdonald C, Actis M, Rodrigues P, Miller DJ, Souphron J, Lewis SM, et al. (2013). Mechanism of ubiquitin ligation and lysine prioritization by a HECT E3. *eLife* 2, e00828. [PubMed: 23936628]
- Kao S-H, Wu H-T, and Wu K-J (2018). Ubiquitination by HUWE1 in tumorigenesis and beyond. *J. Biomed. Sci* 25, 67. [PubMed: 30176860]
- Katiyar S, Liu E, Knutzen CA, Lang ES, Lombardo CR, Sankar S, Toth JI, Petroski MD, Ronai Z, and Chiang GG (2009). REDD1, an inhibitor of mTOR signalling, is regulated by the CUL4A-DDB1 ubiquitin ligase. *EMBO Rep.* 10, 866–872. [PubMed: 19557001]
- Kliza K, and Husnjak K (2020). Resolving the complexity of ubiquitin networks. *Front. Mol. Biosci* 7, 21. [PubMed: 32175328]
- Komander D, and Rape M (2012). The ubiquitin code. *Annu. Rev. Biochem* 81, 203–229. [PubMed: 22524316]
- Krissinel E, and Henrick K (2004). Secondary-structure matching (SSM), a new tool for fast protein structure alignment in three dimensions. *Acta Crystallogr. D Biol. Crystallogr* 60, 2256–2268. [PubMed: 15572779]
- Krissinel E, and Henrick K (2007). Inference of macromolecular assemblies from crystalline state. *J. Mol. Biol* 372, 774–797. [PubMed: 17681537]
- Lee HJ, Li CF, Ruan D, He J, Montal ED, Lorenz S, Girnun GD, and Chan CH (2019). Non-proteolytic ubiquitination of hexokinase 2 by HectH9 controls tumor metabolism and cancer stem cell expansion. *Nat. Commun* 10, 2625. [PubMed: 31201299]

- Legendre-Guillemain V, Wasiak S, Hussain NK, Angers A, and McPherson PS (2004). ENTH/ANTH proteins and clathrin-mediated membrane budding. *J. Cell Sci* 117, 9–18. [PubMed: 14657269]
- Lek M, Karczewski KJ, Minikel EV, Samocha KE, Banks E, Fennell T, O'Donnell-Luria AH, Ware JS, Hill AJ, Cummings BB, et al.; Exome Aggregation Consortium (2016). Analysis of protein-coding genetic variation in 60,706 humans. *Nature* 536, 285–291. [PubMed: 27535533]
- Liu Z, Oughtred R, and Wing SS (2005). Characterization of E3Histone, a novel testis ubiquitin protein ligase which ubiquitinates histones. *Mol. Cell. Biol* 25, 2819–2831. [PubMed: 15767685]
- Lorenz S (2018). Structural mechanisms of HECT-type ubiquitin ligases. *Biol. Chem* 399, 127–145. [PubMed: 29016349]
- Marín I (2010). Animal HECT ubiquitin ligases: evolution and functional implications. *BMC Evol. Biol* 10, 56. [PubMed: 20175895]
- Marín I (2018). Origin and evolution of fungal HECT ubiquitin ligases. *Sci. Rep* 8, 6419. [PubMed: 29686411]
- Mönkemeyer L, Klaips CL, Balchin D, Körner R, Hartl FU, and Bracher A (2019). Chaperone function of Hgh1 in the biogenesis of eukaryotic elongation factor 2. *Mol. Cell* 74, 88–100.e9. [PubMed: 30876804]
- Moortgat S, Berland S, Aukrust I, Maystadt I, Baker L, Benoit V, Caro-Llopis A, Cooper NS, Debray F-G, Faivre L, et al. (2018). HUWE1 variants cause dominant X-linked intellectual disability: a clinical study of 21 patients. *Eur. J. Hum. Genet* 26, 64–74. [PubMed: 29180823]
- Morin A, Eisenbraun B, Key J, Sanschagrin PC, Timony MA, Ottaviano M, and Sliz P (2013). Collaboration gets the most out of software. *eLife* 2, e01456. [PubMed: 24040512]
- O'Connell BC, and Harper JW (2007). Ubiquitin proteasome system (UPS): what can chromatin do for you? *Curr. Opin. Cell Biol* 19, 206–214. [PubMed: 17314036]
- Olivieri M, Cho T, Alvarez-Quilon A, Li K, Schellenberg MJ, Zimmermann M, Hustedt N, Rossi SE, Adam S, Melo H, et al. (2020). A genetic map of the response to DNA damage in human cells. *bioRxiv*. 10.1101/845446.
- Pandya RK, Partridge JR, Love KR, Schwartz TU, and Ploegh HL (2010). A structural element within the HUWE1 HECT domain modulates self-ubiquitination and substrate ubiquitination activities. *J. Biol. Chem* 285, 5664–5673. [PubMed: 20007713]
- Pettersen EF, Goddard TD, Huang CC, Couch GS, Greenblatt DM, Meng EC, and Ferrin TE (2004). UCSF Chimera—a visualization system for exploratory research and analysis. *J. Comput. Chem* 25, 1605–1612. [PubMed: 15264254]
- Prakash S, Tian L, Ratliff KS, Lehotzky RE, and Matouschek A (2004). An unstructured initiation site is required for efficient proteasome-mediated degradation. *Nat. Struct. Mol. Biol* 11, 830–837. [PubMed: 15311270]
- Punjani A, and Fleet DJ (2021). 3D variability analysis: Resolving continuous flexibility and discrete heterogeneity from single particle cryo-EM. *J. Struct. Biol* 213, 107702. [PubMed: 33582281]
- Punjani A, Rubinstein JL, Fleet DJ, and Brubaker MA (2017). cryoSPARC: algorithms for rapid unsupervised cryo-EM structure determination. *Nat. Methods* 14, 290–296. [PubMed: 28165473]
- Punjani A, Zhang H, and Fleet DJ (2020). Non-uniform refinement: adaptive regularization improves single-particle cryo-EM reconstruction. *Nat. Methods* 17, 1214–1221. [PubMed: 33257830]
- Reichen C, Hansen S, and Plückthun A (2014). Modular peptide binding: from a comparison of natural binders to designed armadillo repeat proteins. *J. Struct. Biol* 185, 147–162. [PubMed: 23916513]
- Rohou A, and Grigorieff N (2015). CTFFIND4: fast and accurate defocus estimation from electron micrographs. *J. Struct. Biol* 192, 216–221. [PubMed: 26278980]
- Rosenthal PB, and Henderson R (2003). Optimal determination of particle orientation, absolute hand, and contrast loss in single-particle electron cryomicroscopy. *J. Mol. Biol* 333, 721–745. [PubMed: 14568533]
- Sanchez-Garcia R, Gomez-Blanco J, Cuervo A, Carazo JN, Sorzano COS, and Vargas J (2020). DeepEMhancer: a deep learning solution for cryo-EM volume post-processing. *bioRxiv*. 10.1101/2020.06.12.148296.
- Sander B, Xu W, Eilers M, Popov N, and Lorenz S (2017). A conformational switch regulates the ubiquitin ligase HUWE1. *eLife* 6, e21036. [PubMed: 28193319]

- Scheres SH (2012). RELION: implementation of a Bayesian approach to cryo-EM structure determination. *J. Struct. Biol* 180, 519–530. [PubMed: 23000701]
- Scheres SH, and Chen S (2012). Prevention of overfitting in cryo-EM structure determination. *Nat. Methods* 9, 853–854. [PubMed: 22842542]
- Schneider CA, Rasband WS, and Eliceiri KW (2012). NIH Image to ImageJ: 25 years of image analysis. *Nat. Methods* 9, 671–675. [PubMed: 22930834]
- Schorb M, Haberbosch I, Hagen WJH, Schwab Y, and Mastronarde DN (2019). Software tools for automated transmission electron microscopy. *Nat. Methods* 16, 471–477. [PubMed: 31086343]
- Singh RK, Kabbaj MH, Paik J, and Gunjan A (2009a). Histone levels are regulated by phosphorylation and ubiquitylation-dependent proteolysis. *Nat. Cell Biol* 11, 925–933. [PubMed: 19578373]
- Singh RK, Paik J, and Gunjan A (2009b). Generation and management of excess histones during the cell cycle. *Front. Biosci* 14, 3145–3158.
- Sung MK, Porras-Yakushi TR, Reitsma JM, Huber FM, Sweredoski MJ, Hoelz A, Hess S, and Deshaies RJ (2016). A conserved quality-control pathway that mediates degradation of unassembled ribosomal proteins. *eLife* 5, e19105. [PubMed: 27552055]
- Tan YZ, Baldwin PR, Davis JH, Williamson JR, Potter CS, Carragher B, and Lyumkis D (2017). Addressing preferred specimen orientation in single-particle cryo-EM through tilting. *Nat. Methods* 14, 793–796. [PubMed: 28671674]
- Tanno H, Shigematsu T, Nishikawa S, Hayakawa A, Denda K, Tanaka T, and Komada M (2014). Ubiquitin-interacting motifs confer full catalytic activity, but not ubiquitin chain substrate specificity, to deubiquitinating enzyme USP37. *J. Biol. Chem* 289, 2415–2423. [PubMed: 24324262]
- Thompson JW, Nagel J, Hoving S, Gerrits B, Bauer A, Thomas JR, Kirschner MW, Schirle M, and Luchansky SJ (2014). Quantitative Lys-e-Gly-Gly (diGly) proteomics coupled with inducible RNAi reveals ubiquitin-mediated proteolysis of DNA damage-inducible transcript 4 (DDIT4) by the E3 ligase HUWE1. *J. Biol. Chem* 289, 28942–28955. [PubMed: 25147182]
- Vega-Rubin-de-Celis S, Abdallah Z, Kinch L, Grishin NV, Brugarolas J, and Zhang X (2010). Structural analysis and functional implications of the negative mTORC1 regulator REDD1. *Biochemistry* 49, 2491–2501. [PubMed: 20166753]
- Wagner T, Merino F, Stabrin M, Moriya T, Antoni C, Apelbaum A, Hagel P, Sitsel O, Raisch T, Prumbaum D, et al. (2019). SPHIRE-crYOLO is a fast and accurate fully automated particle picker for cryo-EM. *Commun. Biol* 2, 218. [PubMed: 31240256]
- Walinda E, Morimoto D, Sugase K, Konuma T, Tochio H, and Shirakawa M (2014). Solution structure of the ubiquitin-associated (UBA) domain of human autophagy receptor NBR1 and its interaction with ubiquitin and polyubiquitin. *J. Biol. Chem* 289, 13890–13902. [PubMed: 24692539]
- Wang Z, Michaud GA, Cheng Z, Zhang Y, Hinds TR, Fan E, Cong F, and Xu W (2012). Recognition of the iso-ADP-ribose moiety in poly(ADP-ribose) by WWE domains suggests a general mechanism for poly(ADP-ribosyl)ation-dependent ubiquitination. *Genes Dev.* 26, 235–240. [PubMed: 22267412]
- Wang X, Lu G, Li L, Yi J, Yan K, Wang Y, Zhu B, Kuang J, Lin M, Zhang S, and Shao G (2014). HUWE1 interacts with BRCA1 and promotes its degradation in the ubiquitin-proteasome pathway. *Biochem. Biophys. Res. Commun* 444, 290–295. [PubMed: 24342616]
- Wang Y, Argiles-Castillo D, Kane EI, Zhou A, and Spratt DE (2020). HECT E3 ubiquitin ligases—emerging insights into their biological roles and disease relevance. *J. Cell Sci* 133, jcs228072. [PubMed: 32265230]
- Xu Y, Anderson DE, and Ye Y (2016). The HECT domain ubiquitin ligase HUWE1 targets unassembled soluble proteins for degradation. *Cell Discov.* 2, 16040. [PubMed: 27867533]
- Zheng SQ, Palovcak E, Armache JP, Verba KA, Cheng Y, and Agard DA (2017). MotionCor2: anisotropic correction of beam-induced motion for improved cryo-electron microscopy. *Nat. Methods* 14, 331–332. [PubMed: 28250466]
- Zhong Q, Gao W, Du F, and Wang X (2005). Mule/ARF-BP1, a BH3-only E3 ubiquitin ligase, catalyzes the polyubiquitination of Mcl-1 and regulates apoptosis. *Cell* 121, 1085–1095. [PubMed: 15989957]

- Zhu K, Shan Z, Chen X, Cai Y, Cui L, Yao W, Wang Z, Shi P, Tian C, Lou J, et al. (2017). Allosteric auto-inhibition and activation of the Nedd4 family E3 ligase Itch. *EMBO Rep.* 18, 1618–1630. [PubMed: 28747490]
- Zivanov J, Nakane T, Forsberg BO, Kimanius D, Hagen WJ, Lindahl E, and Scheres SH (2018). New tools for automated high-resolution cryo-EM structure determination in RELION-3. *eLife* 7, e42166. [PubMed: 30412051]
- Zivanov J, Nakane T, and Scheres SHW (2020). Estimation of high-order aberrations and anisotropic magnification from cryo-EM data sets in *RELION-3.1*. *IUCrJ* 7, 253–267.

Highlights

- Structure of a full-length HECT ligase reveals modular assembly
- HUWE1 folds into ring-shaped architecture with flexibly attached accessory domains
- Patient mutations interfere with HUWE1 ligase activity
- Armadillo repeats in the ring architecture contribute to substrate binding

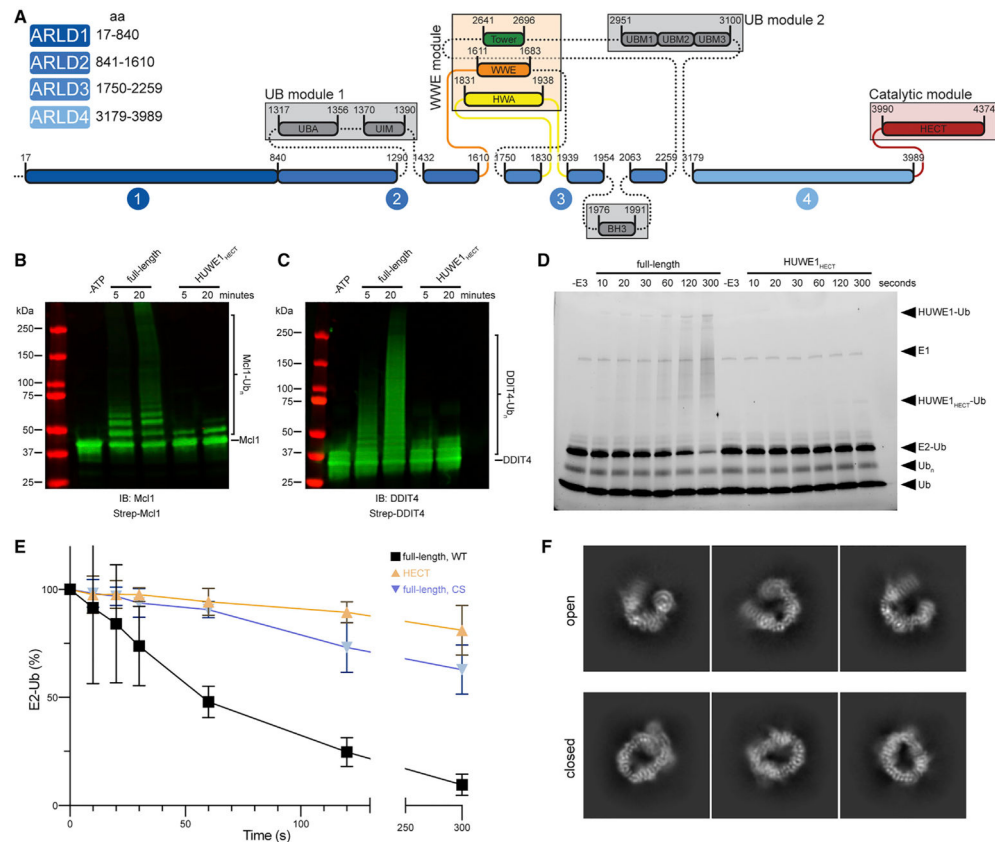


Figure 1. Full-length HUWE1 shows higher activity than isolated HECT domain
 (A) Domain scheme for full-length HUWE1, indicating domain boundaries and amino acids stretched by ARLD1–4. Color scheme is kept constant throughout all figures.
 (B and C) Western blot analysis of *in vitro* ubiquitylation assays with Mcl1 (B) and DDIT4 (C) as substrates. Full-length HUWE1 shows higher activity than HUWE1_{HECT}.
 (D) Single-turnover E2 discharge assay comparing loading of full-length wild-type (WT) and HUWE1_{HECT}. HUWE1_{HECT} is impaired in loading, judged by the disappearance of ubiquitin-charged E2 (E2-Ub) and delayed appearance of ubiquitin-loaded HUWE1_{HECT}-Ub.
 (E) Quantification of single-turnover E2 discharge assay on the basis of three independent replicates for HUWE1 WT, HUWE1_{HECT}, and HUWE1 CS, represented as mean ± SD.
 (F) Representative 2D classes of non-crosslinked HUWE1, revealing at least two distinct overall conformations, one open and flexible and one with a closed ring architecture. The box size is ~280 Å.
 See also Figure S1.

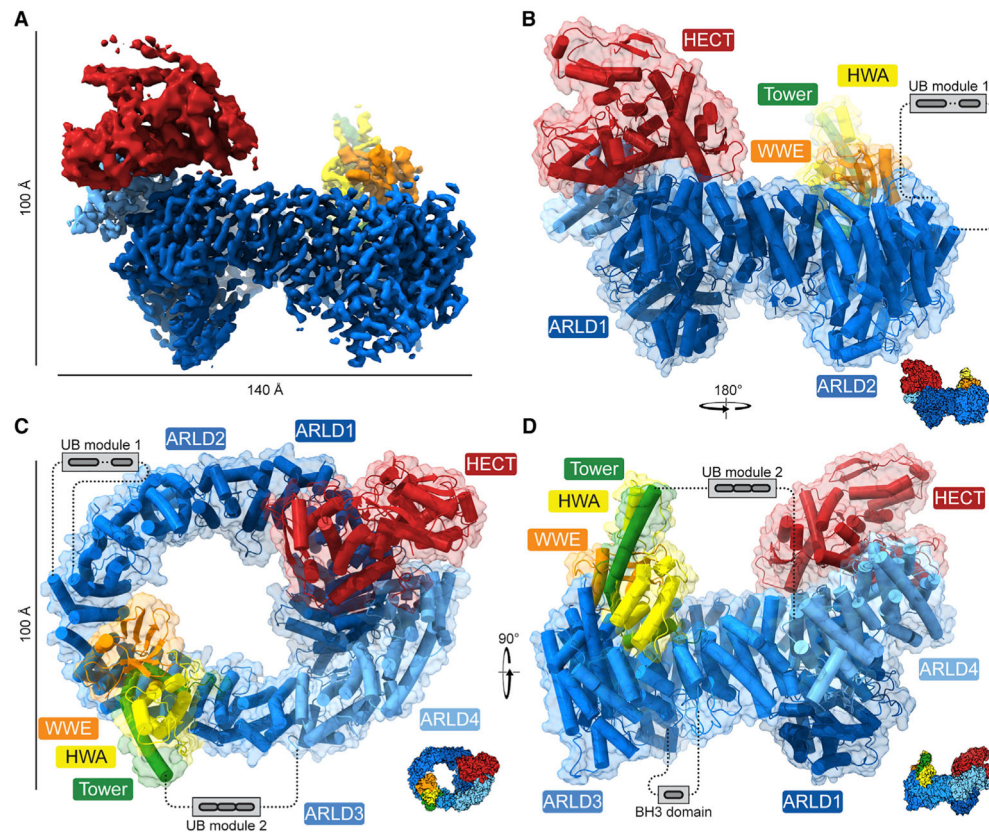


Figure 2. Cryo-EM structure of HUWE1

(A) Composite cryo-EM density, displaying side chain resolution for the helical repeat architecture and lower resolution density for HECT domain and WWE module. Map identity and thresholds for all figures are available in Table S2. The approximate dimensions are indicated in Å.

(B–D) Cartoon representation of HUWE1 with transparent surface. Domains are labeled where applicable, approximate position and anchoring points for mobile domains are indicated, and small cartoons are shown for orientation.

See also Figures S2-S4 and Tables S1 and S2.

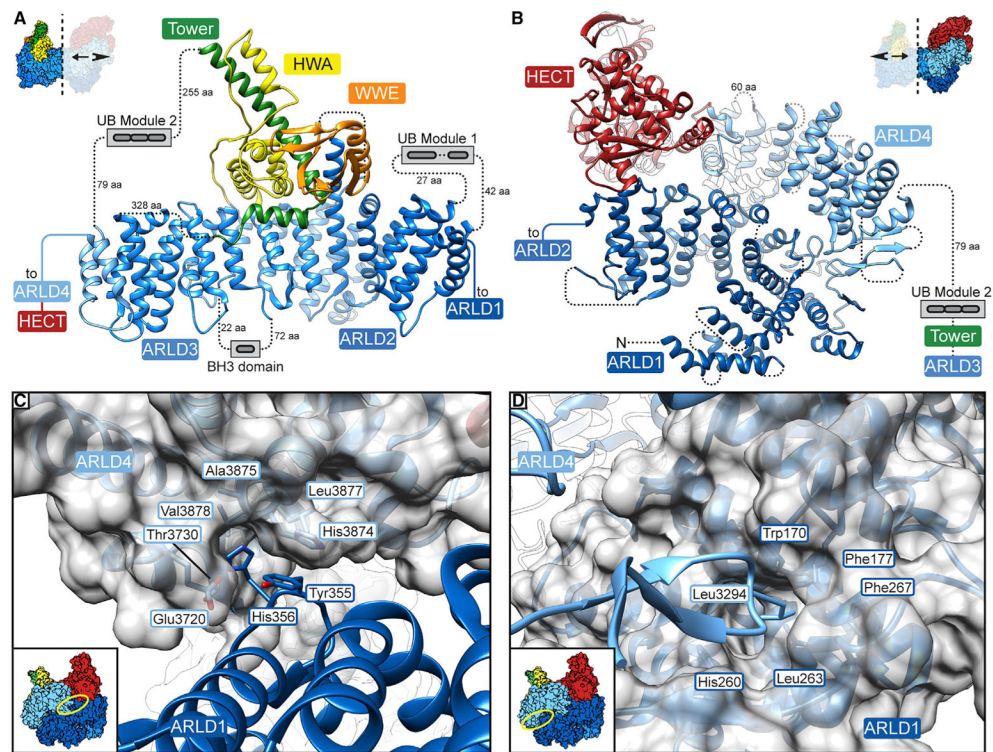


Figure 3. Closed ring architecture of HUWE1

(A and B) Close-up view of HECT-distal (A) and HECT-proximal (B) halves of the HUWE1 structure. Lengths of unresolved linkers (dotted lines) to modules are indicated.

(C) Close-up view of the helix-turn-helix motif (shown as cartoon) with Tyr355 and His356 contacting a hydrophobic groove in ARLD4 (shown as cartoon with transparent surface).

(D) Close-up view of the extended loop (aa 3288–3299) with Leu3294 at its tip (shown as cartoon) protruding into a hydrophobic pocket on ARLD1 (shown as cartoon with transparent surface).

See also Figure S6.

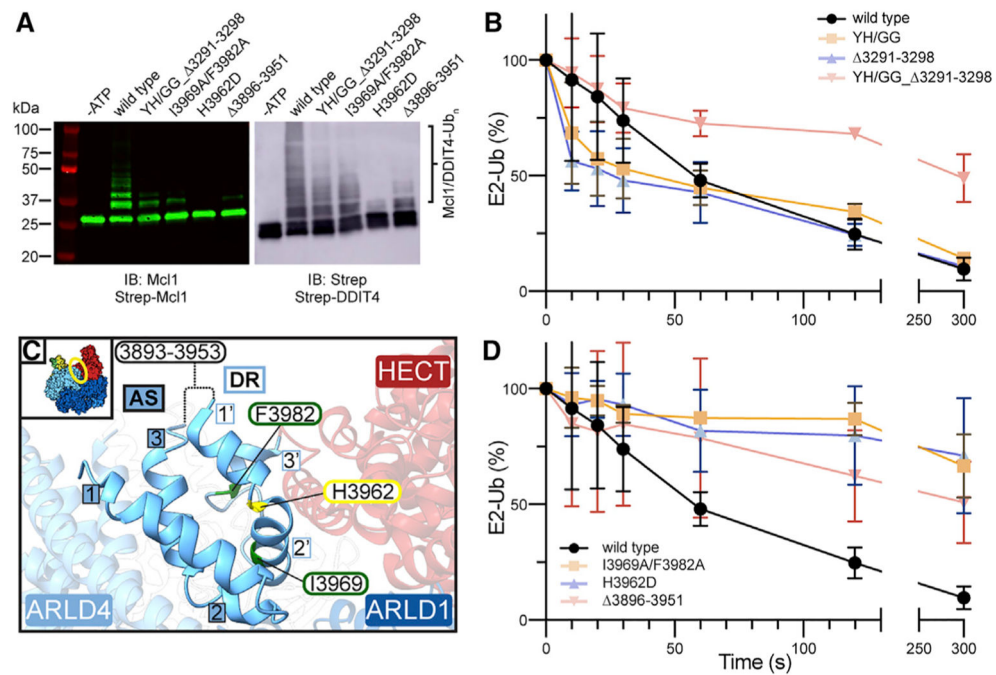


Figure 4. HUWE1 architecture and HECT domain orientation influence activity

(A) *In vitro* ubiquitylation assay for HUWE1 wild-type, for a ring-closure interface mutant (YH/GG_Δ3291–3298) and for variants with mutation in the “dimerization region” (I3969A/F3982A and H3962D). All mutants are impaired in E3 activity on both Mcl1 and DDIT4.

(B) Quantification of single-turnover E2 discharge assay on the basis of three independent replicates for HUWE1 wild-type and three ring-closure interface mutants (YH/GG_Δ3291–3298, and YH/GG_Δ3291–3298), represented as mean ± SD. The double mutant shows significant impairment in ligase loading.

(C) Cartoon representation of HUWE1 illustrating how the HECT domain is linked to the ARLD4 (shown transparent in background). A 3-3 helix bundle (shown solid in foreground) comprising the previously defined “dimerization region” (DR; helices labeled 1’–3’ with white boxes and blue outline) and “activation segment” (AS; helices labeled 1–3 with blue boxes and black outline). The location of the mutants described in (A) and (D) is indicated.

(D) Quantification of single-turnover E2 discharge assay on the basis of three independent replicates for HUWE1 wild-type and mutations in the DR, represented as mean ± SD.

See also Figure S7.

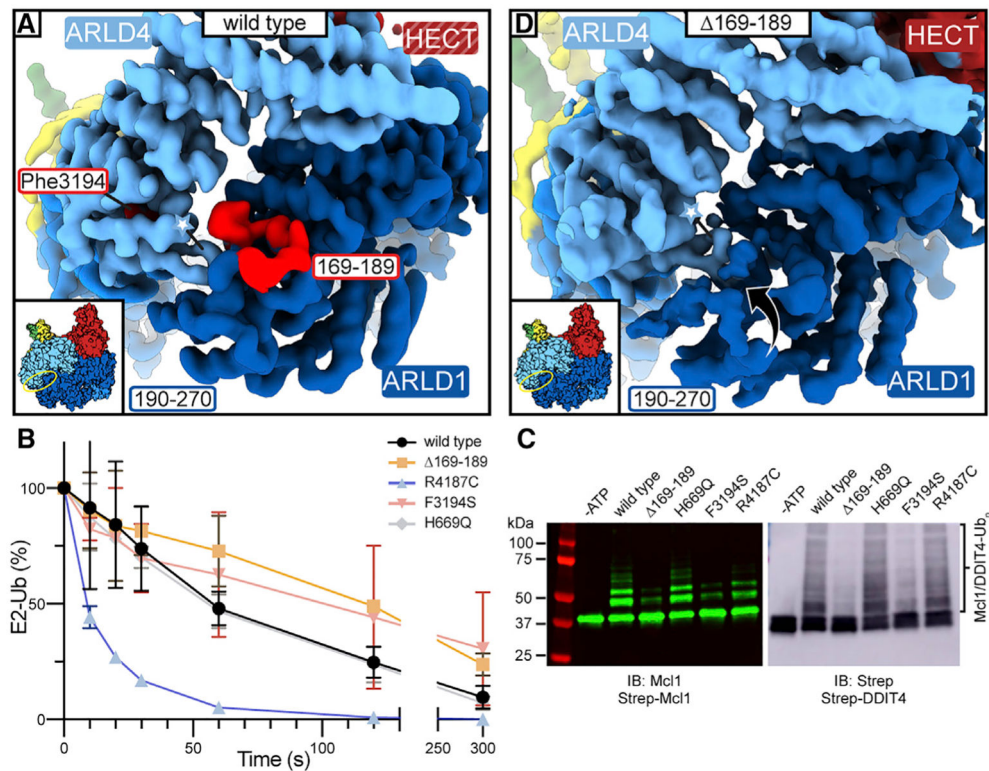


Figure 5. Introducing patient mutations leads to diverse outcomes in activity

(A) Close-up view of the ring-closure interface highlighting the position of the 169–189 class II patient mutation (red). The hydrophobic loop (aa 3288–3299; Figure 3D) making up part of the interface is labeled with a blue asterisk, and the region preceding the patient deletion region (169–189) is indicated (190–270). Cryo-EM density was low-pass-filtered in Chimera using a Gaussian filter at an SD of 1 to visually match the map in (D).

(B) Quantification of single-turnover E2 discharge assay on the basis of three independent replicates for HUWE1 wild-type and HUWE1 with patient mutations from class II (deletion of aa 169–189 (Δ169–189) and F3194S), class III (R4187C), and class IV (H669Q) as indicated. Values are represented as mean ± SD.

(C) *In vitro* ubiquitylation of Mcl1 and DDIT4 by HUWE1 wild-type or HUWE1 with patient mutations as described in (B).

(D) Cryo-EM density of the Δ169–189 mutant, colored according to domains, revealing a remodeled ring-closure interface. Both the hydrophobic loop (aa 3288–3299) as well as the region directly preceding the deletion (aa 190–270) move upward to form the new interface. See also Figures S8 and S9.

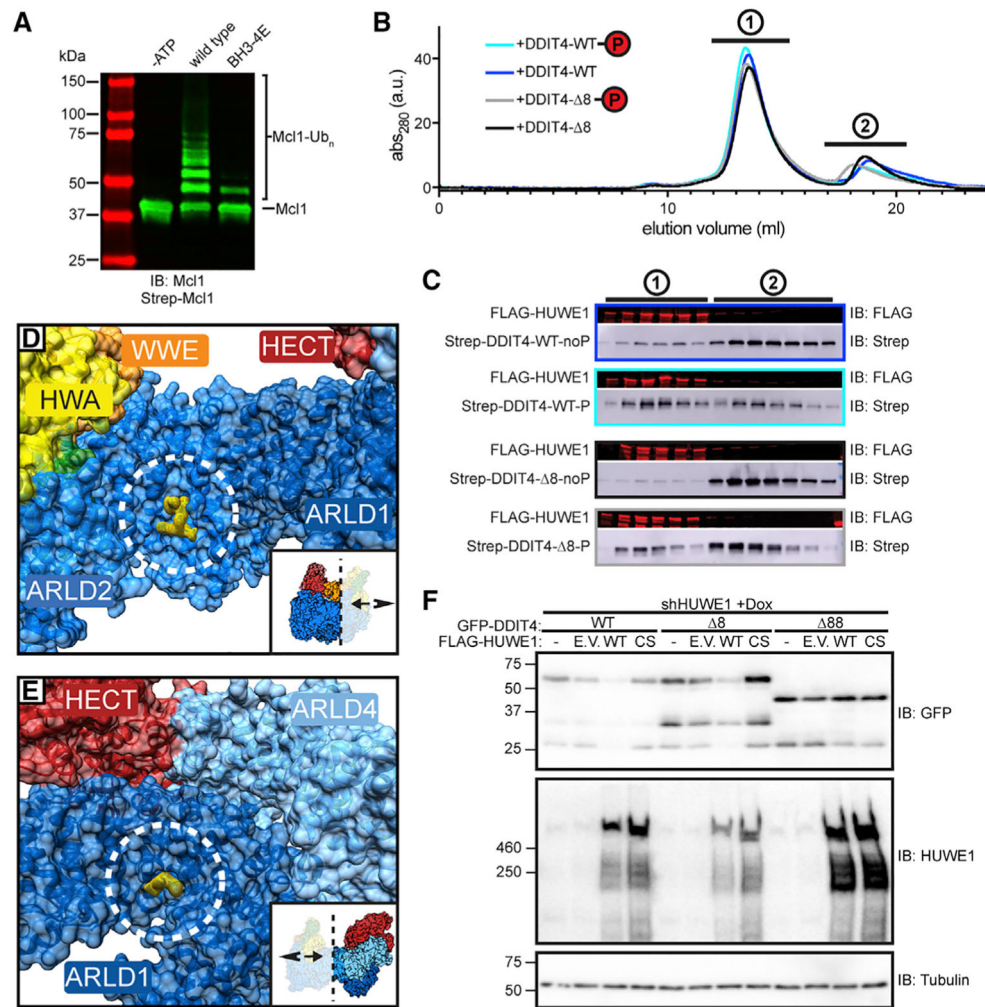


Figure 6. Ring architecture and functional domains are important for activity

(A) *In vitro* ubiquitylation of Mcl1 by wild-type HUWE1 or HUWE1 with mutations in the BH3 domain (V1976E, V1980E, L1983E, M1987E, “BH3-4E”) (Zhong et al., 2005). BH3-4E is impaired in E3 activity.

(B) Chromatography traces (absorption at 280 nm) of SEC co-migration binding assay for HUWE1 incubated with 3:1 molar excess of indicated substrate variants.

(C) Peak fractions (labeled 1 and 2 in B) were separated on SDS-PAGE and analyzed using western blot for the FLAG-tag (HUWE1) and Strep-tags (DDIT4 constructs). Phosphorylated DDIT4 constructs (DDIT4-WT-P and DDIT4-8-P) show higher degree of co-migration with HUWE1 and elute earlier than the corresponding dephosphorylated constructs (DDIT4-WT-noP and DDIT4-8-noP).

(D) Peptide-like additional density found in ARLD2, cryo-EM density shown as yellow mesh on transparent surface.

(E) Peptide-like additional density found in ARLD1, cryo-EM density shown as yellow mesh on transparent surface.

(F) Western blots of 293T cells containing doxycycline-inducible expression of an shRNA targeting HUWE1. As indicated, cells were cultured with or without doxycycline for 2 days

before cotransfection with the indicated variants of GFP-DDIT4 and FLAG-HUWE1. E.V., empty vector; WT, wild-type; CS, HUWE1 C4341S, a catalytically inactive mutant. See also Figures S10-S12.

Author Manuscript

Author Manuscript

Author Manuscript

Author Manuscript

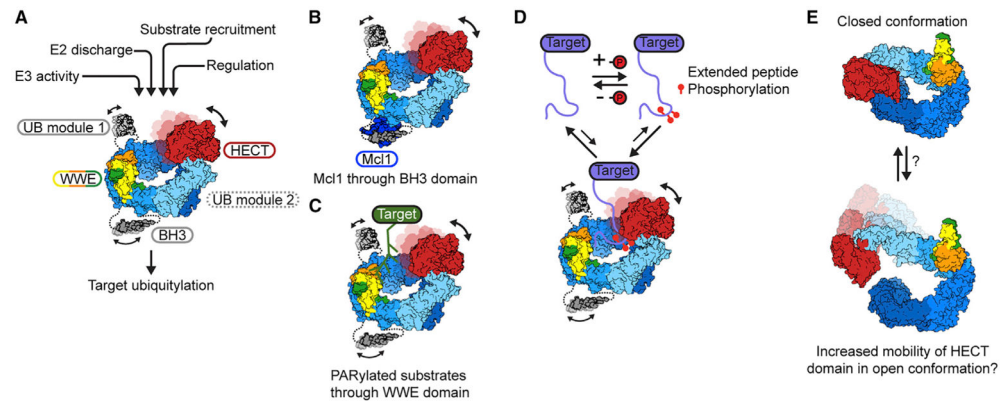


Figure 7. HUWE1 is more than the sum of its parts

(A) In the full-length context, the complete N-terminal region, including protein binding modules and the armadillo-like repeats, influences HUWE1 E3 ligase activity, ligase charging, and substrate recruitment and regulation. Cartoon representation for UB module 2 is omitted for clarity.

(B and C) Target recruitment through dedicated binding domains involves the BH3 domain (B; recruiting Mcl-1) and the WWE module (C; recruiting PARylated substrates).

(D) The helical repeats bind to disordered peptide stretches and read out phosphorylation state. A phosphorylated target has a higher affinity to HUWE1.

(E) HUWE1 potentially exists in an equilibrium between open and closed conformations, and it is likely that multiple conformations are important throughout the substrate ubiquitylation cycle. Opening up the ring architecture results in a large mobility for the HECT domain, while the closed form keeps the HECT domain potentially closer to ARLD1 and the UB module 1.

KEY RESOURCES TABLE

REAGENT or RESOURCE	SOURCE	IDENTIFIER
Antibodies		
anti-Mcl1 rabbit antibody	Cell Signaling Technology	Cat#5453; RRID: AB_10694494
anti-Strep antibody HRP conjugate	Fisher Scientific	Cat#71591-3; RRID: AB_10806716
IRDye800CW Donkey anti-rabbit	LI-COR	Cat#926-32213; RRID: AB_621848
anti-FLAG M2 antibody	Sigma Aldrich	Cat#F3165; RRID: AB_259529
IRDye680 Goat-Anti mouse	LI-COR	Cat#926-68070; RRID: AB_10956588
anti-HUWE1 rabbit antibody	Bethyl	Cat#A300-486; RRID: AB_2264590
anti-GFP mouse antibody	Roche	Cat#11814460001; RRID: AB_390913
ant-tubulin mouse antibody	Cell Signaling Technology	Cat#3873; RRID: AB_1904178
anti-mouse antibody, HRP conjugate	Promega	Cat#W402B; RRID: AB_430834
anti-rabbit antibody, HRP conjugate	Promega	Cat#W401B; RRID: AB_430833
Bacterial and virus strains		
NEB10-beta Competent <i>E. coli</i> cells	New England Biolabs	Cat#C3020K
Chemicals, peptides, and recombinant proteins		
λ -protein phosphatase	New England Biolabs	Cat#P0753S
UBE1	R&D SYSTEMS	Cat#E-304-050
UbcH5b	R&D SYSTEMS	Cat#E2-622-100
Mg-ATP	R&D SYSTEMS	Cat#B-20
Ubiquitin	R&D SYSTEMS	Cat#U-100H-10M
10x E3 Ligase Reaction Buffer	R&D SYSTEMS	Cat#B-71
Ubiquitin N-Terminal Fluorescein	R&D SYSTEMS	Cat#U-580-050
BS3 (bis(sulfosuccinimidyl)suberate)	ThermoFisher Scientific	Cat#21580
Critical commercial assays		
LookOut® Mycoplasma PCR detection kit	Sigma Aldrich	Cat#MP0035-1KT
MycAlert Mycoplasma Detection Kit	Lonza	Cat#LT07-218
Deposited data		
HUWE1, BS3-crosslinked, consensus	this study	EMDB: EMD-22427; PDB: 7JQ9
HUWE1, BS3-crosslinked, focus on HECT	this study	EMDB: EMD-22428; PDB: 7MWD
HUWE1, BS3-crosslinked, focus on WWE	this study	EMDB: EMD-22429; PDB: 7MWE
HUWE1, BS3-crosslinked, focus on interface	this study	EMDB: EMD-22430; PDB: 7MWF
HUWE1, non-crosslinked	this study	EMDB: EMD-22431
HUWE1 169-189	this study	EMDB: EMD-23931
HUWE1-DDIT4 complex	this study	EMDB: EMD-23925; PDB: 7MOP
Gel and western blot source data	this study	Mendeley Data: https://dx.doi.org/10.17632/zj4thx3b4b.1
Experimental models: Cell lines		
Sf9	Expression Systems	Cat#94-001F
Hi5	ThermoFisher Scientific	Cat#B85502
Expi293F	ThermoFisher Scientific	Cat#A14635
239T	ATCC	Cat#CRL-3216

REAGENT or RESOURCE	SOURCE	IDENTIFIER
Recombinant DNA		
pDONR221-HUWE1 isoform2	Addgene	#37431
pDONR221-HUWE1 isoform1	This study	N/A
Original DDIT4 plasmid	Harvard plasmid repository	HsCD00327445
Original Mcl1 plasmid	Harvard plasmid repository	HsCD00004569
pAC8-DDIT4	This study	N/A
pAC8-DDIT4_ 8	This study	N/A
pAC8-Mcl1_ TM	This study	N/A
pAC8-HUWE1 _{HECT}	This study	N/A
pDEST_FLAG-HUWE1	This study	N/A
pDARMO_CMVT_FLAG-HUWE1	This study	N/A
pDONR221-HUWE1_YH/GG	This study	N/A
pDEST_FLAG-HUWE1_YH/GG	This study	N/A
pDONR221-HUWE1_ 3291-3298	This study	N/A
pDEST_FLAG-HUWE1_ 3291-3298	This study	N/A
pDONR221-HUWE1_YH/GG_ 3291-3298	This study	N/A
pDARMO_CMVT_3xFLAG-HUWE1_YH/GG_ 3291-3298	This study	N/A
pDONR221-HUWE1_I3969A/F3982A	This study	N/A
pDARMO_CMVT_3xFLAG-HUWE1_I3969A/F3982A	This study	N/A
pDONR221-HUWE1_H3962D	This study	N/A
pDARMO_CMVT_3xFLAG-HUWE1_H3962D	This study	N/A
pDONR221-HUWE1_ 3896-3951	This study	N/A
pDARMO_CMVT_3xFLAG-HUWE1_ 3896-3951	This study	N/A
pDONR221-HUWE1_ 169-189	This study	N/A
pDARMO_CMVT_3xFLAG-HUWE1_ 169-189	This study	N/A
pDEST_FLAG-HUWE1_ 169-189	This study	N/A
pDONR221-HUWE1_H669Q	This study	N/A
pDARMO_CMVT_3xFLAG-HUWE1_H669Q	This study	N/A
pDONR221-HUWE1_F3194S	This study	N/A
pDEST_FLAG-HUWE1_F3194S	This study	N/A
pDONR221-HUWE1_R4187C	This study	N/A
pDARMO_CMVT_3xFLAG-HUWE1_R4187C	This study	N/A
pDONR221-HUWE1_BH3-4E	This study	N/A
pDEST_FLAG-HUWE1_BH3-4E	This study	N/A
pDONR221-HUWE1_UBA-mut	This study	N/A
pDEST_FLAG-HUWE1_UBA-mut	This study	N/A
pDONR221-HUWE1_UIM-mut	This study	N/A
pDEST_FLAG-HUWE1_UIM-mut	This study	N/A
pDONR221-HUWE1_UBM-mut	This study	N/A
pDEST_FLAG-HUWE1_UBM-mut	This study	N/A
pDONR221-HUWE1_UBA/UIM-mut	This study	N/A
pDEST_FLAG-HUWE1_UBA/UIM-mut	This study	N/A

REAGENT or RESOURCE	SOURCE	IDENTIFIER
pDONR221-HUWE1_UBA/UIM/UBM-mut	This study	N/A
pDEST_FLAG-HUWE1_UBA/UIM/UBM-mut	This study	N/A
pDARMO_CMVT_v1	Addgene	#133072
pDARMO_HUWE1_3xFLAG	This study	N/A
pDEST_GFP_DDIT4	This study	N/A
pDEST_GFP_DDIT4 1-8	This study	N/A
pDEST_GFP_DDIT4 1-88	This study	N/A
pDEST_FLAG_HUWE1 C4341S	This study	N/A
TRIPZ_HUWE1_shRNA_V3THS_353155	Dharmacon	Cat#RHS4696-200765823
Software and algorithms		
SerialEM	Schorb et al., 2019	https://bio3d.colorado.edu/SerialEM/
MotionCor2	Zheng et al., 2017	https://msg.ucsf.edu/
RELION	Scheres, 2012	https://www3.mrc-lmb.cam.ac.uk/relion/
cryoSPARC	Punjani et al., 2017	https://cryosparc.com/
UCSF PYEM	Daniel Asarnow	https://zenodo.org/record/3576630
UCSF Chimera	Pettersen et al., 2004	https://www.cgl.ucsf.edu/chimera/
UCSF ChimeraX	Goddard et al., 2018	https://www.cgl.ucsf.edu/chimerax/
Phenix	Adams et al., 2010	https://phenix-online.org/
Coot	Emsley et al., 2010	https://www2.mrc-lmb.cam.ac.uk/personal/pemsley/coot/
ImageJ	Schneider et al., 2012	https://imagej.nih.gov/ij/
Illustrator	Adobe	https://www.adobe.com
Photoshop	Adobe	https://www.adobe.com
Graphpad prism 7.0	GraphPad	https://www.graphpad.com/
Other		
Quantifoil® R 1.2/1.3 on Cu mesh grids	Quantifoil	Cat#N1-C14nCu30-01
ECL Prime Western Blotting Detection Reagent	GE Healthcare Life Sciences	Cat#RPN2232
Strep-Tactin®XT Superflow® high capacity resin	IBA Lifesciences	Cat#2-4030-025
POROS HQ 50 µm Strong Anion Exchange Resin	Thermo Fisher Scientific	Cat#4467820
Superose 6 10/300 Increase GL	GE Healthcare Life Sciences	Cat#29091596
HiLoad® 16/600 Superdex® 200 pg	GE Healthcare Life Sciences	Cat#29091596